

Primordial non-Gaussianity in the Bispectrum of the Halo Density Field

Tobias Baldauf,^a Uroš Seljak^{a,b,c} and Leonardo Senatore^{d,e}

^aInstitute for Theoretical Physics, University of Zurich, Zurich, Switzerland

^bPhysics Department, Astronomy Department and Lawrence Berkeley National Laboratory, University of California, Berkeley, CA, USA

^cInstitute for the Early Universe, Ewha Womans University, Seoul, South Korea

^dStanford Institute for Theoretical Physics, Stanford University, Stanford, CA, USA

^eKavli Institute for Particle Astrophysics and Cosmology, Menlo Park, CA, USA

E-mail: baldauf@physik.uzh.ch

Abstract. The bispectrum vanishes for linear Gaussian fields and is thus a sensitive probe of nonlinearities and non-Gaussianities in the cosmic density field. Hence, a detection of the bispectrum in the halo density field would enable tight constraints on non-Gaussian processes in the early Universe and allow inference of the dynamics driving inflation. We present a tree level derivation of the halo bispectrum arising from non-linear clustering, non-linear biasing and primordial non-Gaussianity. A diagrammatic description is developed to provide an intuitive understanding of the contributing terms and their dependence on scale, shape and the non-Gaussianity parameter f_{NL} . We compute the terms based on a multivariate bias expansion and the peak-background split method and show that non-Gaussian modifications to the bias parameters lead to amplifications of the tree level bispectrum that were ignored in previous studies. Our results are in a good agreement with published simulation measurements of the halo bispectrum. Finally, we estimate the expected signal to noise on f_{NL} and show that the constraint obtainable from the bispectrum analysis significantly exceeds the one obtainable from the power spectrum analysis.

Keywords: Inflation, Large Scale Structure, Primordial non-Gaussianity

Contents

1	Introduction	1
2	Basics	2
3	Bias from the Universal Mass Function	4
3.1	Mass Functions	4
3.2	Multivariate Lagrangian Bias	6
3.3	Transformation to Eulerian Space	7
4	Perturbation Theory including non-Gaussianity	9
4.1	Matter Density Field	9
4.2	Halo Density Field	10
4.3	Diagrammatic Representation	11
4.4	Feynman Rules for the n -Spectra	13
4.5	Matter Power Spectrum	14
4.6	Matter Bispectrum	14
5	Bispectra of Biased Tracers	15
5.1	Halo Bispectrum	15
5.2	Cross-Bispectra	18
5.3	Discussion of the Results	19
5.4	Comparison to Simulations	22
6	Signal-to-Noise	24
7	Conclusions	26
A	Standard Perturbation Theory	30

1 Introduction

The question whether the inhomogeneities in our Universe have been seeded by a Gaussian initial distribution raised a lot of excitement recently (see [1, 2] for reviews). Inflation [3–5] is a theoretical paradigm that could generate the initial fluctuations, but has not yet been directly confirmed observationally. Standard slow-roll inflation predicts a very low level of non-Gaussianity. However, there is no shortage of single and multifield inflationary models with most of them predicting a fluctuation distribution distinct from the simple Gaussian case. Thus detection of a non-Gaussian signal would provide unprecedented information about the dynamics driving inflation and the interactions of the inflaton field [6].

The fluctuations in the inflaton field are imprinted in the distribution of photons and matter in the Universe. This raises the question of which observable is best suited to detect the tiny deviations from the fiducial Gaussian distribution of field amplitudes. Certainly, it is promising to look at statistics that would vanish in the Gaussian case, such as the bispectrum of the Cosmic Microwave Background (CMB) radiation that for a long time was believed to be the most promising probe of primordial non-Gaussianity [7]. In Large Scale Structure (LSS) the detection of primordial non-Gaussianity is hampered by the non-Gaussianity produced by late time non-linear clustering, a caveat not present in the linear CMB physics. Only in recent years it was realised that equally strong constraints can be obtained from the LSS [8]. One of the most promising features of primordial non-Gaussianity in the LSS is the scale dependence of the halo bias. This scale dependent bias is most prominent for non-Gaussianities with non-vanishing squeezed limit of the bispectrum, such as the

local shape [9, 10] and the shapes with both equilateral and local limit recently found in the Effective Theory of Multifield Inflation [11]. It was theoretically predicted for the local type non-Gaussianity by [12] and subsequently other derivations were presented by [13, 14]. These were confirmed in simulations by [12, 15–20]. First data analysis based on the scale dependent non-Gaussian bias lead to remarkably strong constraints on local non-Gaussianity [14].

The two point function and its Fourier transform, the power spectrum, are the most important statistics that have been used to analyse LSS surveys so far. Their drawback in terms of the detection of non-Gaussianities is that the signatures may be small and difficult to separate from non-Gaussianities generated by gravity, whereas the distinct features of alternative inflationary models will be imprinted more clearly in higher order statistics such as the three point function or the bispectrum

$$\langle \delta(\mathbf{k}_1)\delta(\mathbf{k}_2)\delta(\mathbf{k}_3) \rangle = (2\pi)^3 \delta^{(D)}(\mathbf{k}_1 + \mathbf{k}_2 + \mathbf{k}_3) B(\mathbf{k}_1, \mathbf{k}_2, \mathbf{k}_3), \quad (1.1)$$

which vanish for Gaussian fields. Measuring the higher order statistics is more involved than the standard power spectrum analysis because these statistics show both shape and scale dependence, and both of these dependencies need to be considered in order to constrain different forms of primordial non-Gaussianity. In this paper we try to address whether bispectrum analysis can improve on the power spectrum analysis of LSS surveys in terms of detecting primordial non-Gaussianity of the local type.

In [21] it was proven that the optimal estimator of non-Gaussianity is the bispectrum. This raises the question how the power spectrum could possibly give tighter constraints than the bispectrum. In the analysis of LSS surveys it is extremely difficult to extract information from the very high- k non-linear modes. This restricts the analysis of the bispectrum to relatively low- k modes that are sufficiently linear. The situation is changed when one considers biased tracers of the density field. These can be related to bispectrum [22], hence they trace non-Gaussian information. The bias effectively allows us to extract some of the non-Gaussian information in the high- k modes from the power spectrum analysis. This effectively increases the number of modes in the survey, and allows to tighten the limits on the non-Gaussian parameters. Still, one would expect that the bispectrum analysis contains further information and the question is how it compares to the power spectrum analysis of biased tracers.

For simplicity, we will focus our attention on the local type of non-Gaussianity, where the potential shows a self coupling that is local in real space. The local shape of non-Gaussianity is for instance predicted by multi-field inflation [23–25] and in the bouncing cosmology model [26]. Recently [11] found new shapes with none vanishing squeezed limit whose LSS phenomenology is yet to be derived.

This paper breaks down as follows. We first review the basics of non-Gaussianity in Section 2 and then describe the multivariate biasing scheme and peak-background split approach previously introduced by [14, 27] in Section 3. Section 4 introduces the perturbative solutions for the distribution of matter and biased tracers as well as our new diagrammatic prescription for the calculation of their n -spectra. Section 5 is devoted to the calculation of the halo bispectrum whose constraining power is compared to the power spectrum in Section 6. We conclude our findings in Section 7.

2 Basics

We consider the local type of non-Gaussianity [9, 10, 28, 29]

$$\Phi_{\text{nG}}(\mathbf{x}) = \varphi(\mathbf{x}) + f_{\text{NL}} (\varphi^2(\mathbf{x}) - \langle \varphi^2 \rangle) + g_{\text{NL}} \varphi^3(\mathbf{x}), \quad (2.1)$$

where φ is an auxiliary primordial Gaussian potential.¹ Following the peak-background split approach [14] we consider the potential as a superposition of small and large scale modes $\varphi = \varphi_s + \varphi_l$ separated

¹ The coupling of the potentials in Eq. (2.1) is naturally imposed in the early Universe during Inflation. This approach, which is followed by our study, is denoted the CMB convention. However, some authors impose the same equation in the late time evolved Universe (the LSS convention). Therefore one has to be careful when comparing quoted constraints on the non-Gaussianity parameters. Namely, the potential evolves as

$$\varphi(\mathbf{x}, a) = \frac{D(a)}{a} \varphi(\mathbf{x}, a_0 = 1) = g(a) \varphi(\mathbf{x}, a_0 = 1), \quad (2.2)$$

by a cut-off wavelength Λ . Thus from Eq. (2.1) one obtains

$$\Phi_{\text{nG}} = \varphi_1 + f_{\text{NL}}\varphi_1^2 + g_{\text{NL}}\varphi_1^3 + (1 + 2f_{\text{NL}}\varphi_1 + 3g_{\text{NL}}\varphi_1^2)\varphi_s + (f_{\text{NL}} + 3g_{\text{NL}}\varphi_1)\varphi_s^2 + g_{\text{NL}}\varphi_s^3, \quad (2.3)$$

where all the fields are evaluated at the same spatial position \mathbf{x} . Short modes in the above expression can be easily identified since only terms containing at least one Gaussian short mode can contribute to the short wavelength power. These short wavelength modes dominate the collapse of dark matter haloes, whereas the long wavelength modes raise or lower the actual density in large patches of the sky, effectively lowering and raising the collapse threshold. In the presence of non-Gaussianity the long wavelength modes furthermore affect the variance of the short modes and thus lead to an additional dependence of the number density of collapsed objects on the amplitude of the long wavelength modes. As we will see, in the presence of local non-Gaussianities, this effect is proportional to the value of the long wavelength Newtonian potential, leading to a distinct scale dependent effect.

The actual effect of the long mode on the variance of the non-Gaussian short modes can be estimated as follows. Squaring the short part of the non-Gaussian potential we obtain

$$\Phi_{\text{nG},s}^2 = (1 + 4f_{\text{NL}}\varphi_1 + 6g_{\text{NL}}\varphi_1^2 + 4f_{\text{NL}}^2\varphi_1^2 + 12f_{\text{NL}}g_{\text{NL}}\varphi_1^3 + 9g_{\text{NL}}^2\varphi_1^4)\varphi_s^2, \quad (2.4)$$

of which we can easily compute the expectation over the short modes

$$\sigma_{\text{nG},s}^2 = \langle \Phi_{\text{nG},s}^2 \rangle_s = (1 + 4f_{\text{NL}}\varphi_1 + 6g_{\text{NL}}\varphi_1^2 + 4f_{\text{NL}}^2\varphi_1^2 + 12f_{\text{NL}}g_{\text{NL}}\varphi_1^3 + 9g_{\text{NL}}^2\varphi_1^4)\sigma_{\text{G},s}^2, \quad (2.5)$$

where we identified $\sigma_{\text{G},s}^2 = \langle \varphi_s^2 \rangle_s$. Here we neglect all correlators of odd number of φ_s as well as the $\sigma_{\text{G},s}^4 = \langle \varphi_s^4 \rangle$ term. The resulting expression agrees with the expressions previously derived by [12, 14]. In contrast to the variance, the three point function or skewness

$$\langle \Phi_{\text{nG},s}^3 \rangle_s = 6f_{\text{NL}}\langle \varphi_s^2 \rangle_s^2(1 + 4f_{\text{NL}}\varphi_1) + 6g_{\text{NL}}\langle \varphi_s^2 \rangle_s^2\varphi_1 \quad (2.6)$$

vanishes in the Gaussian case. Similar to the variance, the skewness is rescaled by the long wavelength potential.

Now it remains to connect the non-Gaussian effects on the gravitational potential to the distribution of matter. In the Newtonian limit, valid well inside the horizon, the Poisson equation relates the long wavelength Gaussian potential to the density perturbation,

$$\Phi(\mathbf{k}) = \frac{\delta_{\text{p}}(\mathbf{k}, z)}{\alpha(k, z)}, \quad (2.7)$$

where we introduced the auxiliary function²

$$\alpha(k, z) = \frac{2k^2 c^2 D(z) T(k)}{3H_0^2 \Omega_{\text{m}}} \frac{g(z=0)}{g(z_{\infty})}, \quad (2.8)$$

which scales as k^2/H^2 on large scales where the transfer function is unity. As discussed in [30–32], on horizon scales unphysical gauge modes and relativistic corrections to the Poisson equation require a more careful analysis. Fig. 1 shows the Poisson factor as a function of k -mode. Note that the corrections to the Gaussian spectra are given as powers of $f_{\text{NL}}/\alpha(k)$. The importance of potential and density terms is equal at $k \approx 2 \times 10^{-4} \text{ hMpc}^{-1}$ for $f_{\text{NL}} = \mathcal{O}(1)$ and at $k \approx 2 \times 10^{-3} \text{ hMpc}^{-1}$ for $f_{\text{NL}} = \mathcal{O}(100)$. Here and in the rest of the paper we use the transfer function for a cosmology with $\Omega_{\text{m}} = 0.25$, $\Omega_{\Lambda} = 0.75$, $\sigma_8 = 0.8$, $n_{\text{s}} = 1.0$.

where $D(a)$ is the linear growth factor normalised to unity at $a_0 = 1$ and thus $g(a_0 = 1) = 1$. In an Einstein-de-Sitter Universe the potential is constant in time, whereas it decays as $g(a=0)/g(a_0=1) = 1.34 \approx 4/3$ in the currently favoured Λ CDM model.

²Note that we are not writing explicitly the norm of a vector but use the notation $k = |\mathbf{k}|$

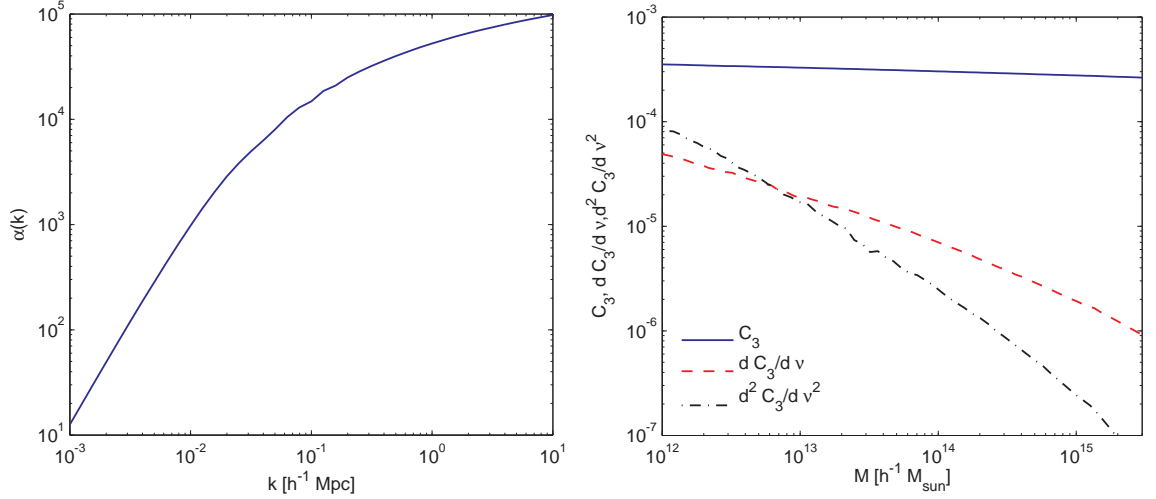


Figure 1. *Left panel:* Poisson factor $\alpha(k)$ relating density and potential via $\delta(k) = \alpha(k)\Phi(k)$. On scales of $k \approx 0.1 \, h\text{Mpc}^{-1}$ the potential is smaller than the density by a factor of 10^5 , whereas they are equal on very large scales of $k \approx 2 \times 10^{-4} \, h\text{Mpc}^{-1}$. The non-Gaussian corrections generally scale as $f_{\text{NL}}/\alpha(k)$ and are thus suppressed on high k 's. Note that the Poisson equation in Newtonian gauge receives general relativistic corrections as $\alpha(k)$ approaches unity. *Right panel:* Skewness $C_3 = \sigma S_3$ and its first and second mass derivatives evaluated for $f_{\text{NL}} = 1$ and $\varphi_1 = 0$.

3 Bias from the Universal Mass Function

Galaxies and their host haloes are believed to trace a smoothed version of the underlying distribution of dark matter. The relation between the local overdensity in the matter and halo fields is described by the bias function. This bias function can be related to the abundance of haloes of mass M described by the halo mass function. In this Section we will review the basic Gaussian mass functions and their non-Gaussian corrections. Finally, we will present the peak-background split and multivariate biasing scheme previously introduced by [14, 27].

3.1 Mass Functions

Haloes are assumed to form at the peaks of the underlying dark matter density field. Numerical simulations and analytical calculations indicate that the abundance of collapsed objects can be inferred from the distribution of points that exceed the density threshold $\delta_c = 1.686$. Following the first studies of [33] (hereafter PS) it was found that the mass function, the number density of collapsed objects of mass M , reduces to an universal functional form for different redshifts and cosmologies if it is expressed in terms of the peak height

$$\nu = \left(\frac{\delta_c}{\sigma_{\text{NG}}} \right)^2, \quad (3.1)$$

where $\sigma(M)$ is the variance of the density field smoothed on mass scale M . Then the number of collapsed objects of mass M can be expressed as

$$n(M) = \nu f(\nu) \frac{\bar{\rho}}{M^2} \frac{d \ln \nu}{d \ln M}. \quad (3.2)$$

Using a random walk in a Gaussian density field PS derived

$$\nu f(\nu) = \sqrt{\frac{\nu}{2\pi}} \exp \left[-\frac{\nu}{2} \right], \quad (3.3)$$

which is however not in very good agreement with the mass function measured in numerical simulations. To improve the agreement, [34] (hereafter ST) proposed a modified version of the Press-Schechter mass function

$$\nu f(\nu) = A(p) \left(1 + \frac{1}{(q\nu)^p}\right) \sqrt{\frac{q\nu}{2\pi}} \exp\left[-\frac{q\nu}{2}\right], \quad (3.4)$$

where the parameters $q = 0.707$ and $p = 0.3$ were obtained from a fit to numerical simulations and A is a normalisation factor.

Performing the random walk using non-Gaussian statistics is more involved, however using an Edgeworth expansion of the exponential [35] (hereafter LV) obtained for the mass function

$$n_{LV}(M) = \sqrt{\frac{2}{\pi}} \frac{\bar{\rho}}{M} \exp\left[-\frac{\delta_c^2}{2\sigma^2}\right] \left[\frac{d \ln \sigma}{dM} \left(\frac{\delta_c}{\sigma} + \frac{S_3 \sigma}{6} \left(\frac{\delta_c^4}{\sigma^4} - 2 \frac{\delta_c^2}{\sigma^2} - 1 \right) \right) + \frac{1}{6} \frac{dS_3}{dM} \sigma \left(\frac{\delta_c^2}{\sigma^2} - 1 \right) \right], \quad (3.5)$$

where the skewness is defined as

$$S_3 = \frac{\langle \delta_M^3 \rangle_c}{\langle \delta_M^2 \rangle_c^2}. \quad (3.6)$$

The above derivation based on the Edgeworth expansion is expected to be satisfactory for low peaks only. In the case of local type non-Gaussianity we obtain for the skewness

$$C_3 = \sigma_G S_3 = \frac{6f_{NL}}{\sigma_G^3} \int \frac{d^3 q}{(2\pi)^3} \int \frac{d^3 q'}{(2\pi)^3} \alpha_M(\mathbf{q}) \alpha_M(\mathbf{q}') \alpha_M(\mathbf{q} + \mathbf{q}') P_{\varphi\varphi}(\mathbf{q}) P_{\varphi\varphi}(\mathbf{q}'), \quad (3.7)$$

where $\alpha_M(k) = W_M(k) \alpha(k)$ and $W_M(k)$ is the filter of mass scale M . The LV mass function in Eq. (3.5) is not in the form of an universal mass function. We can however rewrite it simply applying the chain rule to σS_3 .

$$\begin{aligned} n_{LV}(M) &= \sqrt{\frac{1}{2\pi}} \frac{\bar{\rho}}{M^2} \exp\left[-\frac{\delta_c^2}{2\sigma^2}\right] \frac{d \ln \nu}{d \ln M} \left[\frac{\delta_c}{\sigma} + \frac{S_3 \sigma}{6} \left(\frac{\delta_c^4}{\sigma^4} - 3 \frac{\delta_c^2}{\sigma^2} \right) - \frac{1}{3} \frac{dS_3 \sigma}{d\nu} \left(\frac{\delta_c^4}{\sigma^4} - \frac{\delta_c^2}{\sigma^2} \right) \right] \\ &= n_{PS}(M) \left[1 + \frac{S_3 \sigma}{6} \left(\nu^{3/2} - 3\nu^{1/2} \right) - \frac{1}{3} \frac{dS_3 \sigma}{d\nu} \left(\nu^{3/2} - \nu^{1/2} \right) \right] \\ &= n_{PS}(M) R(\nu), \end{aligned} \quad (3.8)$$

where we introduced the auxiliary function

$$R(\nu) = 1 + \frac{S_3 \sigma}{6} \left(\nu^{3/2} - 3\nu^{1/2} \right) - \frac{1}{3} \frac{dS_3 \sigma}{d\nu} \left(\nu^{3/2} - \nu^{1/2} \right). \quad (3.9)$$

The presence of the σS_3 terms still spoils the universality because this term carries a mass dependence via the smoothing scale. As shown in [16] and in Fig. 1, σS_3 is only very weakly dependent on the smoothing radius, such that we can safely treat it as a constant in the mass function.

Thus we managed to write the non-Gaussian mass function in the form of an universal mass function and can benefit from the known results for universal mass functions. Usually the LV mass function is multiplied by a correction factor $\gamma(M) = n_{ST}(M)/n_{PS}(M)$ to improve the agreement with simulations, leading to $n_{LV}(M) = n_{ST}(M) R(\nu)$. The underlying assumption is that ST corrects PS for triaxial collapse and LV corrects PS for non-Gaussianity.³ Alternative derivations of non-Gaussian mass functions that are valid in various, if not all, regimes have been presented by [36, 37]. For our study, the important result following from these analyses is that to a good approximation, all of the above mass functions can be treated as universal, that is as being function of δ_c/σ only, and that the inferred values of the biases are not very different.

³It is not clear how well this statement is theoretically justified, by it is enough for us for obtaining an estimate on the non-Gaussian effects on the mass function and the induced biases.

3.2 Multivariate Lagrangian Bias

The spherical top hat collapse model states that a spherical overdensity collapses to form a gravitationally bound object once it exceeds a certain overdensity threshold δ_c . Long wavelength density perturbations raise or lower the mean density in a patch of the Universe and thus effectively raise or lower the collapse threshold $\delta_c \rightarrow \delta_c - \delta_1$. So far, the bias parameters were calculated by expanding the local number density in the amplitude of the long wavelength density fluctuation only. As we saw above, coupling between long and short modes leads to an enhancement of the variance of the short wavelength density perturbations affecting the peak height ν . This enhancement is proportional to the long wavelength Gaussian potential. This suggests to calculate the distribution of collapsed objects by expanding the local number density in terms of the long wavelength modes of both density and potential as previously noted by [14, 27, 38]

$$n(\mathbf{x}) = \bar{n} + \frac{\partial n}{\partial \delta_1} \delta_1(\mathbf{x}) + \frac{\partial n}{\partial \varphi_1} \varphi_1(\mathbf{x}) + \frac{1}{2} \frac{\partial^2 n}{\partial \delta_1^2} \delta_1^2(\mathbf{x}) + \frac{2}{2!} \frac{\partial^2 n}{\partial \delta_1 \partial \varphi_1} \delta_1(\mathbf{x}) \varphi_1(\mathbf{x}) + \frac{1}{2} \frac{\partial^2 n}{\partial \varphi_1^2} \varphi_1^2(\mathbf{x}) \quad (3.10)$$

here we write down explicitly the spatial dependence to highlight the local relation between bias, overdensity and potential. The multivariate bias expansion is not stating that density and potential are independent parameters, but rather that the different scale dependence of density and potential requires one to expand in both of them in order to keep the bias parameters scale independent. As we will stress at the end of this subsection, it is important that these fields are restricted to long-wavelengths. Notice that the fact that the overdensity depends locally only on δ and φ is a consequence of the functional dependence of the mass function on δ and φ even in the non-Gaussian case. Defining $\delta_h(\mathbf{x}) = n(\mathbf{x})/\bar{n} - 1$ and identifying the partial derivatives with the bias parameters we obtain in Lagrangian space

$$\delta_h^L(\mathbf{x}) = b_{10}^L \delta_0(\mathbf{x}) + b_{01}^L \varphi(\mathbf{x}) + \frac{b_{20}^L}{2!} \delta_0^2(\mathbf{x}) + b_{11}^L \delta_0(\mathbf{x}) \varphi(\mathbf{x}) + \frac{b_{02}^L}{2!} \varphi^2(\mathbf{x}) + \dots, \quad (3.11)$$

where δ_0 is the initial Lagrangian overdensity.

Assuming that the local number density can be expressed with an universal mass function as in Eq. (3.2), we can write the Lagrangian bias parameters as

$$b_{10}^L = \frac{1}{\bar{n}} \frac{\partial n}{\partial \delta_1} = -\frac{1}{\bar{n}} \frac{2\nu}{\delta_c} \frac{\partial n}{\partial \nu} \quad (3.12)$$

$$b_{01}^L = \frac{1}{\bar{n}} \frac{\partial n}{\partial \varphi_1} = -\frac{4f_{\text{NL}}\nu}{\bar{n}} \frac{\partial n}{\partial \nu} = 2f_{\text{NL}}\delta_c b_{10}^L \quad (3.13)$$

$$b_{20}^L = \frac{1}{\bar{n}} \frac{\partial^2 n}{\partial \delta_1^2} = \frac{4}{\bar{n}} \frac{\nu^2}{\delta_c^2} \frac{\partial^2 n}{\partial \nu^2} + \frac{2}{\bar{n}} \frac{\nu}{\delta_c^2} \frac{\partial n}{\partial \nu} \quad (3.14)$$

$$b_{11}^L = \frac{1}{\bar{n}} \frac{\partial^2 n}{\partial \varphi_1 \partial \delta_1} = \frac{8f_{\text{NL}}}{\bar{n}} \left(\frac{\nu^2}{\delta_c} \frac{\partial^2 n}{\partial \nu^2} + \frac{\nu}{\delta_c} \frac{\partial n}{\partial \nu} \right) \quad (3.15)$$

$$= 2f_{\text{NL}} (\delta_c b_{20}^L - b_{10}^L) \quad (3.16)$$

$$b_{02}^L = \frac{1}{\bar{n}} \frac{\partial^2 n}{\partial \varphi_1^2} = \frac{8f_{\text{NL}}^2}{\bar{n}} \left(2\nu^2 \frac{\partial^2 n}{\partial \nu^2} + 3\nu \frac{\partial n}{\partial \nu} \right) - \frac{12\nu g_{\text{NL}}}{\bar{n}} \frac{\partial n}{\partial \nu} \quad (3.17)$$

$$= 4f_{\text{NL}}^2 \delta_c (b_{20}^L \delta_c - 2b_{10}^L) + 6\delta_c g_{\text{NL}} b_{10}^L \quad (3.18)$$

We left the derivatives of the mass function unevaluated and obtained expressions that are sufficiently general to enable application to different Gaussian and non-Gaussian mass functions. For instance, the derivatives of the ST mass function Eq. (3.4) are given by

$$\frac{1}{n_{\text{ST}}} \frac{\partial n_{\text{ST}}}{\partial \nu} = -\frac{q\nu - 1}{2\nu} - \frac{p}{\nu(1 + (q\nu)^p)} \quad (3.19)$$

$$\frac{1}{n_{\text{ST}}} \frac{\partial^2 n_{\text{ST}}}{\partial \nu^2} = \frac{p^2 + \nu pq}{\nu^2(1 + (q\nu)^p)} + \frac{(q\nu)^2 - 2q\nu - 1}{4\nu^2} \quad (3.20)$$

and for the LV mass function Eq. (3.8) by

$$\frac{1}{n_{\text{LV}}} \frac{\partial n_{\text{LV}}}{\partial \nu} = \frac{1}{n_{\text{ST}}} \frac{\partial n_{\text{ST}}}{\partial \nu} + \frac{1}{R} \frac{\partial R(\nu)}{\partial \nu} \quad (3.21)$$

$$\frac{1}{n_{\text{LV}}} \frac{\partial^2 n_{\text{LV}}}{\partial \nu^2} = \frac{1}{n_{\text{ST}}} \frac{\partial^2 n_{\text{ST}}}{\partial \nu^2} + 2 \frac{1}{n_{\text{ST}} R} \frac{\partial n_{\text{ST}}}{\partial \nu} \frac{\partial R(\nu)}{\partial \nu} + \frac{1}{R} \frac{\partial^2 R(\nu)}{\partial \nu^2}. \quad (3.22)$$

As we will explain in more detail in the next section, the peak-background split method assumes long wavelength modes as a homogeneous rescaling, so it works in the limit of infinitely long smoothing scale, *i.e.* $\Lambda = 0$. Since in this limit there is no perturbation theory to do, this means that the bias parameters we obtain from the peak background split method are the renormalized ones [38, 39], in the sense that perturbation theory loop-diagrams involving bias vertices (see the next section for the definition of the bias vertices) have been already resummed inside the renormalized bias parameters. Although this statement has not been carefully verified from a theoretical point of view, it seems in accord with what is inferred from simulations. In fact in [12, 14, 40], a good agreement between peak background split predictions for b_{10} , b_{20} and b_{01} and simulations has been found. There is evidence for a weak dependence of these parameters on the smoothing scale, but it has been shown that the bias in Fourier space is well approximated by the local bias model [41]. Since the fact that the peak background split method gives directly the renormalized bias parameters is independent of the assumption of Gaussian initial conditions, it is not unreasonable to assume that this fact also extends to the non-Gaussian bias parameters b_{02} , b_{11} , \dots used in our study. The derivation presented so far assumes a universal mass function, *i.e.* that all the dependence on the long modes is implicitly encoded in the peak height ν . However, intrinsically non-Gaussian properties of the distribution enter in the non-Gaussian mass function, for example $S_3\sigma$ in the case of the LV mass function. Following an argument similar to the one we used to derive the φ_1 dependence of the variance in Eq. (2.5), one can show based on Eq. (2.6) that the three point function in the presence of a long fluctuation gets rescaled as $\langle \delta_M^3 \rangle \rightarrow \langle \delta_M^3 \rangle (1 + 4f_{\text{NL}}\varphi_1)$. This dependence on φ_1 can not be encoded in ν and thus an additional explicit derivative with respect to the long wavelength potential arises, which leads to the following corrections to the bias parameters, for example for the LV mass function:

$$\Delta b_{01} = \frac{2}{3} \frac{f_{\text{NL}} C_3}{R} \left(\nu^{3/2} - 3\nu^{1/2} \right) \quad (3.23)$$

$$\Delta b_{11} = -\frac{2}{3} \frac{f_{\text{NL}} C_3 \nu}{R \delta_c} \left[\frac{1}{n_{\text{ST}}} \frac{\partial n_{\text{ST}}}{\partial \nu} \left(\nu^{3/2} - 3\nu^{1/2} \right) + \frac{3}{2} \left(\nu^{1/2} - \nu^{-1/2} \right) \right] \quad (3.24)$$

$$\Delta b_{02} = -\frac{16}{3} \frac{f_{\text{NL}}^2 \nu C_3}{R} \left[\frac{1}{n_{\text{ST}}} \frac{\partial n_{\text{ST}}}{\partial \nu} \left(\nu^{3/2} - 3\nu^{1/2} \right) + \frac{3}{2} \left(\nu^{1/2} - \nu^{-1/2} \right) \right] \quad (3.25)$$

These corrections are generally of the same order as the bias corrections arising from the non-Gaussian LV mass function in Eq. (3.21) and (3.22). However, for high ν the latter dominate. For realistic values of f_{NL} all the bias corrections arising from the non-Gaussian mass function are on the percent level. The mass function itself can be trusted at the 10% level only and thus these corrections can be safely neglected.

3.3 Transformation to Eulerian Space

Observations are performed in the late time evolved Eulerian density field. It thus remains to translate the above result to Eulerian space. The halo density fields in Eulerian and Lagrangian space are related by [42]

$$(1 + \delta_{\text{h}}^{\text{E}}) = (1 + \delta)(1 + \delta_{\text{h}}^{\text{L}}). \quad (3.26)$$

Finally, one wants to write down the Eulerian analogue of Eq. (3.11)

$$\delta_{\text{h}}^{\text{E}}(\mathbf{x}) = b_{10}^{\text{E}} \delta(\mathbf{x}) + b_{01}^{\text{E}} \varphi(\mathbf{x}) + \frac{b_{20}^{\text{E}}}{2!} \delta^2(\mathbf{x}) + b_{11}^{\text{E}} \delta(\mathbf{x}) \varphi(\mathbf{x}) + \frac{b_{02}^{\text{E}}}{2!} \varphi^2(\mathbf{x}) + \dots \quad (3.27)$$

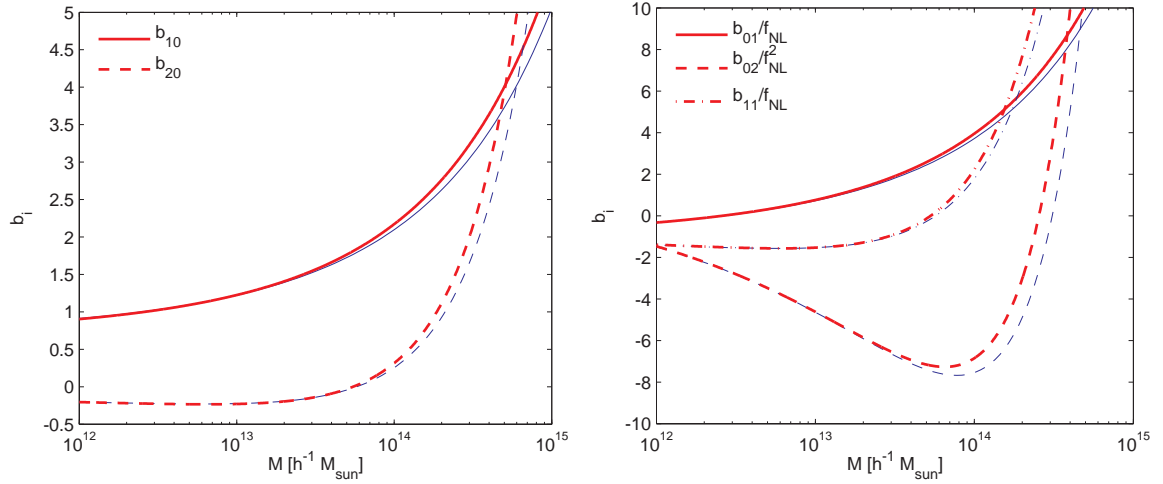


Figure 2. Eulerian multivariate bias parameters for $f_{\text{NL}} = 100$, $g_{\text{NL}} = 0$. *Left panel:* Bias parameters for δ . *Right panel:* Bias parameters for φ . For $g_{\text{NL}} = 0$ one has $b_{02} \propto f_{\text{NL}}^2$, $b_{01} \propto f_{\text{NL}}$, $b_{11} \propto f_{\text{NL}}$ and thus the rescaled bias parameters are independent of f_{NL} . b_{02} shown by the dashed line shows a pronounced minimum for $M \approx 1 \times 10^{14} h^{-1} M_{\odot}$ that is multiplied by f_{NL}^2 and can thus lead to a large contribution. The red lines are derived from the ST mass function, whereas the blue thin lines are derived from the LV mass function including the explicit φ_1 correction of Eqs. (3.23), (3.24) and (3.25).

In what follows we will absorb the prefactors in the bias parameters, thus $b_{20}/2! \rightarrow b_{20}$ and $b_{02}/2! \rightarrow b_{02}$. The linearly evolved Lagrangian overdensity can be expanded in powers of the final Eulerian overdensity

$$\delta_0 = \sum_i a_i \delta^i = a_1 \delta + a_2 \delta^2 + a_3 \delta^3 + \dots \quad (3.28)$$

where the expansion parameters a_i are given by the spherical collapse dynamics $a_1 = 1$, $a_2 = -17/21$, $a_3 = 341/567$. We calculated the corresponding Eulerian bias parameters using the relations in [27, 42, 43]

$$b_{10}^{\text{E}} = 1 + b_{10}^{\text{L}} \quad (3.29)$$

$$b_{20}^{\text{E}} = 2(a_1 + a_2)b_{10}^{\text{L}} + a_1^2 b_{20}^{\text{L}} \quad (3.30)$$

$$b_{01}^{\text{E}} = b_{01}^{\text{L}} \quad (3.31)$$

$$b_{02}^{\text{E}} = b_{02}^{\text{L}} \quad (3.32)$$

$$b_{11}^{\text{E}} = b_{11}^{\text{L}} a_1 + b_{01}^{\text{L}} \quad (3.33)$$

Calculations of the evolved density field are most conveniently done in Fourier space. Thus we translate the above expansion Eq. (3.27) to k -space.

$$\delta_{\text{h}}(\mathbf{k}) = b_{10}^{\text{E}} \delta(\mathbf{k}) + b_{01}^{\text{E}} \varphi(\mathbf{k}) + b_{20}^{\text{E}} [\delta * \delta](\mathbf{k}) + b_{11}^{\text{E}} [\delta * \varphi](\mathbf{k}) + b_{02}^{\text{E}} [\varphi * \varphi](\mathbf{k}), \quad (3.34)$$

where we introduced the notation $[\delta * \delta](\mathbf{k})$ as a shorthand for the convolution integral. From now on we will omit the superscript E and all bias factors should be understood as the Eulerian ones.

In Fig. 2 we show the mass dependence of the bias parameters arising from the Gaussian ST and the non-Gaussian LV mass function. The bias factors of the potential and the density-potential cross term are scaled by their f_{NL} dependence. From this figure it is obvious that the second order biases can be negative over large parts of the interesting mass range. This can lead to subtle cancellations between terms in the resulting galaxy or halo n -point functions. Furthermore, the f_{NL}^2 dependence and the pronounced minimum in $b_{02}(M)$ around $M = 10^{14} h^{-1} M_{\odot}$ can boost the corresponding terms on large scales. As noted already by [15] and apparent in Fig. 2, the non-Gaussian mass function

Eq. (3.8) leads to an additional scale independent offset in the bias. From Fig. 2 we see that the difference in the bias parameters is most apparent for high mass haloes, whereas there is only a small difference for low mass haloes. The differences between the bias from the two mass functions are very small and negligible for our purposes. The same is approximately true even for the other non-Gaussian mass functions. Thus we use the Gaussian ST mass function for our numerical predictions.

4 Perturbation Theory including non-Gaussianity

4.1 Matter Density Field

Perturbation theory (PT) aims to solve the cosmological fluid equations using an expansion about the linear overdensity $\delta_m^{(1)}(\mathbf{k})$ [44]

$$\delta_m(\mathbf{k}) = \delta_m^{(1)}(\mathbf{k}) + \delta_m^{(2)}(\mathbf{k}) + \delta_m^{(3)}(\mathbf{k}) + \dots \quad (4.1)$$

In our approach, these modes should be thought of as having wavelength longer than the cutoff Λ^{-1} that separates short and long modes. Let us define a linearly evolved primordial density field (*i.e.* evolved without taking into account the gravitational evolution), to be $\delta_{m,p}$. At first order, $\alpha(k, z)\varphi(\mathbf{k}) = \delta_{m,p}^{(1)}(\mathbf{k}, z)$, *i.e.* the primordial Gaussian potential φ is of the same order as the primordial linear overdensity $\delta_{m,p}^{(1)}$. In the following we refer to these two quantities as first order quantities and count the order of terms by counting the powers of first order terms.

The non-Gaussian self-coupling of the potential introduces non-linearities in the evolved primordial density field, whereas in the Gaussian case we would have $\delta_{m,p} = \delta_{m,p}^{(1)}$. Transforming Eq. (2.1) to Fourier space and applying Eq. (2.7) we obtain for the linearly evolved primordial matter density up to third order

$$\delta_{m,p}(\mathbf{k}, z) = \alpha(k, z)\Phi(\mathbf{k}) \quad (4.2)$$

$$\begin{aligned} &= \alpha(k, z)\varphi(\mathbf{k}) + \alpha(k, z)f_{\text{NL}} \int \frac{d^3q}{(2\pi)^3} \varphi(\mathbf{q})\varphi(\mathbf{k} - \mathbf{q}) \\ &+ \alpha(k, z)g_{\text{NL}} \int \frac{d^3q}{(2\pi)^3} \int \frac{d^3q'}{(2\pi)^3} \varphi(\mathbf{q})\varphi(\mathbf{q}')\varphi(\mathbf{k} - \mathbf{q} - \mathbf{q}'), \end{aligned} \quad (4.3)$$

$$= \delta_{m,p}^{(1)}(\mathbf{k}, z) + f_{\text{NL}}\delta_{m,p}^{(2)}(\mathbf{k}, z) + g_{\text{NL}}\delta_{m,p}^{(3)}(\mathbf{k}, z). \quad (4.4)$$

The resulting field is then subject to late-time non-linear gravitational clustering, which introduces further couplings. To take this effect into account we use the evolved primordial distribution as the source for the late time evolution and insert Eq. (4.4) into the known PT expressions for $\delta_m^{(1)}$, $\delta_m^{(2)}$ and $\delta_m^{(3)}$ (see appendix A)

$$\delta_{m,nG}^{(1)}(\mathbf{k}, z) = \delta_{m,p}^{(1)}(\mathbf{k}, z), \quad (4.5)$$

$$\begin{aligned} \delta_{m,nG}^{(2)}(\mathbf{k}, z) &= \int \frac{d^3q}{(2\pi)^3} \delta_{m,p}^{(1)}(\mathbf{q})\delta_{m,p}^{(1)}(\mathbf{k} - \mathbf{q})F_2(\mathbf{q}, \mathbf{k} - \mathbf{q}) \\ &+ f_{\text{NL}}\delta_{m,p}^{(2)}(\mathbf{k}, z), \end{aligned} \quad (4.6)$$

$$\begin{aligned} \delta_{m,nG}^{(3)}(\mathbf{k}, z) &= \int \frac{d^3q}{(2\pi)^3} \int \frac{d^3q'}{(2\pi)^3} \delta_{m,p}^{(1)}(\mathbf{q}, z)\delta_{m,p}^{(1)}(\mathbf{q}', z)\delta_{m,p}^{(1)}(\mathbf{k} - \mathbf{q} - \mathbf{q}', z)F_3(\mathbf{q}, \mathbf{q}', \mathbf{k} - \mathbf{q}) \\ &+ f_{\text{NL}} \int \frac{d^3q}{(2\pi)^3} \delta_{m,p}^{(1)}(\mathbf{q}, z)\delta_{m,p}^{(2)}(\mathbf{k} - \mathbf{q}, z)F_2(\mathbf{q}, \mathbf{k} - \mathbf{q}) \\ &+ g_{\text{NL}}\delta_{m,p}^{(3)}(\mathbf{k}, z), \end{aligned} \quad (4.7)$$

where $F_2(\mathbf{k}_1, \mathbf{k}_2)$ and $F_3(\mathbf{k}_1, \mathbf{k}_2, \mathbf{k}_3)$ are the standard second and third order mode coupling kernels.

4.2 Halo Density Field

The halo density including higher order corrections from biasing, non-Gaussianity and non-linear clustering can be derived using Eq. (4.1) in Eq. (3.34)

$$\begin{aligned}
\delta_h(\mathbf{k}) = & b_{10} \left(\delta_{m,nG}^{(1)}(\mathbf{k}) + \delta_{m,nG}^{(2)}(\mathbf{k}) \right) + b_{01} \varphi(\mathbf{k}) \\
& + b_{20} [\delta_{m,nG}^{(1)} * \delta_{m,nG}^{(1)}](\mathbf{k}) + b_{11} [\delta_{m,nG}^{(1)} * \varphi](\mathbf{k}) + b_{02} [\varphi * \varphi](\mathbf{k}) \\
= & b_{10} \delta_{m,p}^{(1)}(\mathbf{k}) + b_{01} \varphi(\mathbf{k}) \\
& + b_{02} \int \frac{d^3 q}{(2\pi)^3} \varphi(\mathbf{q}) \varphi(\mathbf{k} - \mathbf{q}) + b_{20} \int \frac{d^3 q}{(2\pi)^3} \delta_{m,p}^{(1)}(\mathbf{q}) \delta_{m,p}^{(1)}(\mathbf{k} - \mathbf{q}) \\
& + b_{10} \int \frac{d^3 q}{(2\pi)^3} \delta_{m,p}^{(1)}(\mathbf{q}) \delta_{m,p}^{(1)}(\mathbf{k} - \mathbf{q}) F_2(\mathbf{q}, \mathbf{k} - \mathbf{q}) + \alpha(k) f_{NL} b_{10} \int \frac{d^3 q}{(2\pi)^3} \varphi(\mathbf{q}) \varphi(\mathbf{k} - \mathbf{q}) \\
& + b_{11} \int \frac{d^3 q}{(2\pi)^3} \delta_{m,p}^{(1)}(\mathbf{q}) \varphi(\mathbf{k} - \mathbf{q}).
\end{aligned} \tag{4.8}$$

Note that at lowest order we recover the well known result of [12]

$$\delta_h(\mathbf{k}) = \left(b_{10} + \frac{2f_{NL}\delta_c(b_{10} - 1)}{\alpha(k)} \right) \delta_{m,p}(\mathbf{k}). \tag{4.10}$$

At this order the potential can be replaced by the density due to the linearity of the Poisson equation in k -space. Thus one finally obtains an expression that is proportional to the density, but non-local. The next to leading order, however, is not proportional to $\delta^2(\mathbf{k})$ since the density and the potential are convolved with each other. It is due to this effect that the bias expansion should be performed both in δ and φ .

We would like to stress an important subtlety concerning the usage of the biases obtained from the peak background split method in perturbation theory. Depending on the precision required for the calculation, it is possible that higher order corrections from perturbation theory need to be implemented. In the diagrammatic description, which is explained in the next subsection, there are loop diagrams (convolutions of the fields with some kernel) involving non-linear bias vertices and other diagrams involving only matter fields and matter vertices.⁴ Unfortunately, these diagrams are in general highly dependent on the cutoff Λ (*i.e.* the smoothing scale). Clearly, physical quantities do not depend on the smoothing scale. This spurious dependence can be removed by defining effective or, more precisely, *renormalized* bias parameters that take into account both the tree level contributions and the loop contributions and that are directly connected to observable quantities. These renormalized parameters do not depend on the smoothing scale, while the coupling constants with which we perform perturbation theory and the contributions from loop diagrams do depend on the cutoff Λ . This process is familiar in quantum field theory. Now, in performing any form of perturbation theory, there are diagrams that involve non-linear bias vertices as part of the loops. They contribute to physical quantities effectively renormalising the linear bias. For example, it is possible to show that loop corrections to the power spectrum originating for example from b_{20} and b_{30} terms effectively renormalize b_{10} and b_{01} [45, 46].⁵ As mentioned in the former section, the biases as inferred by the peak background split method should be interpreted as the renormalized ones. Therefore, diverging

⁴This statement is made precise by saying that if we concentrate on One Particle Irreducible (1PI) diagrams, there are diagrams involving non-linear bias vertices and others without bias vertices.

⁵In fact, it is easy to estimate the one loop contribution due to b_{20} combined with an f_{NL} vertex and an F_2 vertex (see next section for these definitions). This diagram induces an effective bias b_{01} numerically equivalent to the one we obtain with the peak-background split if we consider small external k 's, the very high mass scale and most importantly the smoothing scale is equal to the mass scale of the halo [47]. This is an effect that arises from pushing the smoothing scale to very high k 's, where it is unclear whether perturbative calculations can be trusted. Moreover, two terms agree only in the high mass limit.

diagrams⁶ involving non-linear bias parameters in the loops in perturbation theory have been already accounted for and we need to consider only the non-divergent loop diagrams that are finite on large scales. This guarantees that the tree level calculation presented here gives the dominant contribution on large scales. This is an important subtlety that arises from having taken the biases from the peak background split method and that simplifies the calculation of the large scale observables. Finally, it should be stressed that even the remaining perturbation theory should be performed in a way that ensures that the remaining contributions do not depend on the smoothing length Λ^{-1} . This forces to use a carefully defined perturbation theory, such as for example ‘renormalized perturbation theory’ [48], or the recently proposed effective fluid description of cosmological perturbations [49].

4.3 Diagrammatic Representation

In the previous section we derived the perturbative expressions for the matter and halo density fields. As a consequence of the stochastic nature of cosmological fluctuations, there is no hope to directly predict the observed distribution of galaxies and matter in the Universe. Rather, we need to calculate expectation values of products of the fields and compare them to the corresponding statistics as measured in the sky. The calculation of these statistics turns out to be an involved combinatorial task if one goes beyond second order in the fields.

To facilitate these calculations, we present a diagrammatic representation of the mode coupling terms that arise from biasing, non-linear clustering and non-Gaussianity. Similar diagrammatic representations of perturbation theory have been used in the literature [44, 50–52] but we are not aware of an intuitive inclusion of all the three effects into one prescription. These Feynman diagrams show intuitively which coupling terms arise and can be translated into the corresponding equations by straightforward application of a set of Feynman rules.

Let us start representing the fields, as the basic ingredients of the theory. What we want to calculate in the end are correlators of halo or matter density fields, thus we need symbols for the outer points, namely δ_h and δ_m . The latter two are represented by the half filled and filled circles depicted in Fig. 3. Note that when δ_m is used for an outer point it always includes all the possible non-Gaussian and non-linear contributions up to the considered order, whereas the density as a source field is linear. Next, we consider the primordial potential φ , represented by an open circle. Even if $\alpha(k)\varphi(\mathbf{k}) = \delta_{m,p}^{(1)}(\mathbf{k})$, we introduce symbols for both the density and potential to make the $1/k^2$ behaviour of the potential terms more obvious and to make sure that the potential terms arise only directly from the initial conditions. However, no difference is made between the evolved primordial and the late time non-linear matter density field in terms of the symbols, because they can be distinguished from the context. For instance, the coupling vertices for gravity are sourced by evolved primordial matter fields defined in Eq. (4.4) and lead to non-linear fields (see the discussion of the vertices below for more details). Finally, the initial conditions are known in terms of the power spectra of fluctuations. Thus we also introduce the power spectrum symbolised by the half filled big circle, where subscripts are used to distinguish the density-density, density-potential and potential-potential power spectra.



Figure 3. Symbols use to represent the fields and power spectra. From left to right, the primordial Gaussian potential φ , the matter density field δ_m , the galaxy/halo density field δ_h , and the power spectrum $P(k)$ arising from two linked fields.

The non-linear clustering vertices (we will refer to them also as gravity vertices) F_i , coupling two matter density fields, are represented by the open squares shown in Fig. 4. The input density field on

⁶Diagrams leading to an unweighted integral over the power spectrum $\int d^3q/(2\pi)^3 P(q) = \sigma^2$ where the upper limit of integration is on very high wavenumbers. From the peak-background split we get the biases renormalized at infinite smoothing length. It is possible that loops with momenta running up to the smoothing scale involving bias vertices are necessary to obtain the correct biases. However they are small and for our purposes negligible. A better understanding of this point lies beyond the scope of the current paper.

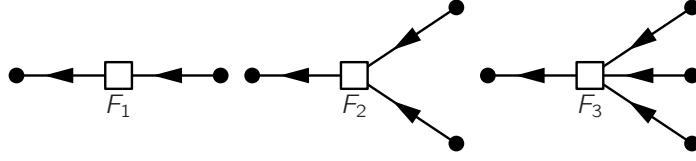


Figure 4. Non-linear gravitational clustering leads to a convolution integral weighted by a F_i kernel, which we symbolise by a square shaped vertex. From left to right we show the first, second and third order mode coupling contributions to the matter density field. Note that $F_1 \equiv 1$.

the right hand side is an evolved primordial field $\delta_{m,p}$ defined in Eq. (4.4), which receives higher order corrections from non-Gaussianity only. Fig. 5 shows the vertices arising from the multivariate bias expansion, where the input can be a matter density field of any order or the primordial potential. The identification of the higher order bias terms with vertices is possible, since in k -space the products of fields lead to convolution integrals, which are similar to the non-linear gravity terms, where the F_i kernels are replaced by the scale independent bias factors b_{ij} . Thus we interpret biasing as an unweighted convolution of source modes. As noted above, loop diagrams involving higher order bias vertices can thus lead to large or divergent contributions, effectively renormalising lower order bias parameters. Similarly, the non-Gaussian terms are effectively coupling potential modes to a higher order primordial matter mode $\delta_{m,p}^{(n)}$. This interaction is represented by the diamond shaped open vertices depicted in Fig. 6, corresponding to $\alpha(k)Q_{NL}$, where $Q_{NL} = \{e_{NL}, f_{NL}, \dots\}$.

Time integration is trivially performed in standard perturbation theory since all the initial fields are linearly evolved, considering only the growing mode. Thus the lines correspond to propagators, *i. e.* linear growth factors. However, these linear growth factors can be used to transform the initial fields to linearly evolved fields such that we can totally ignore the time evolution as long as we use linearly evolved primordial matter fields as a source. We only need to ensure causality by following the time evolution of the fields. Non-Gaussian coupling happens directly after inflation, then non-linear clustering and finally biasing. The lines used to connect the primordial potential with the non-Gaussian vertices and the non-Gaussian bias vertices are dashed to highlight the fact that the coupling of primordial potentials, and thus the imprint of non-Gaussianity, happens directly after inflation. To facilitate the distinction of the density propagators, we use straight and wiggly lines for the matter and halo density field, respectively.

The i -th order contribution to an evolved matter or halo field can be obtained following the time evolution step by step starting from the initial conditions and going all the way to the final field

1. Draw i initial fields $\delta_{m,p}^{(1)}$ or φ .
2. Draw the non-Gaussian Q_{NL} vertices and connect them to the primordial potential using dashed lines.
3. Draw the gravity vertices and connect them to the non-Gaussian vertices or initial density fields by solid lines.
4. For biased tracers, draw the bias vertices and connect them to either initial density fields, gravity vertices, non-Gaussian vertices or primordial potentials. Use a wiggly line to connect them with the outer point.

So far we focused our attention on the fields. To compute the i -th order contribution⁷ to the n -spectra we need to glue n diagrams with i source fields and n outer points in all possible ways and then pair the source fields in all possible ways. Two linked source fields lead to a power spectrum and a momentum conserving delta function $\langle \delta(\mathbf{k})\delta(\mathbf{k}') \rangle = (2\pi)^3 \delta^{(D)}(\mathbf{k} + \mathbf{k}') P_{\delta\delta}(k)$. The potential-potential and density-potential power spectra are related to the density-density power spectra by the appropriate Poisson factors $\alpha(k, z)$. For the translation of the above diagrams into mathematical

⁷The index i has to be even since the correlator of an odd number of Gaussian fields vanishes due to the Wick-theorem

expressions we assign k -vectors to each of the outer fields. The different ways of performing this assignment are accounted for by the cyclic permutations of the k -vectors.

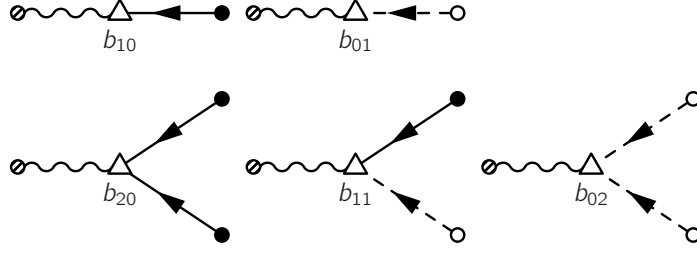


Figure 5. The multivariate bias expansion can be expressed by the triangular vertices shown above. The interaction of two fields on a vertex corresponds to a convolution integral over the ingoing k -vectors without any weighting. The vertex is connected to the outer point by the wiggly halo propagator. Ingoing potentials are always primordial because the coupling of long and short modes, and thus the enhancement of the short wavelength variance, happens in the early Universe.

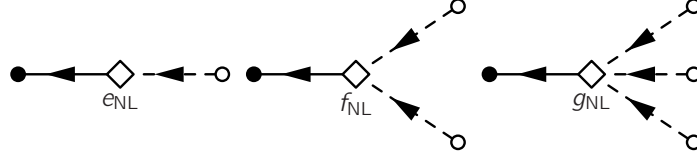


Figure 6. The non-Gaussian vertices correspond to an unweighted convolution integral times one factor of α and the corresponding $Q_{\text{NL}} = \{e_{\text{NL}}, f_{\text{NL}}, \dots\}$. We introduce the e_{NL} vertex to represent the conversion from φ to $\delta_{\text{m,p}}^{(1)}$. Note that the ingoing potentials are always primordial, which is highlighted by the dashed line.

4.4 Feynman Rules for the n -Spectra

Even though the diagrams can be straightforwardly translated into the corresponding mathematical expressions we write down the Feynman rules explicitly for the sake of definiteness. For the calculation of the i -th order contribution to the n -spectrum do the following

1. Draw all distinct connected diagrams with n external lines up to the desired order i in φ
 - i.) For each vertex with ingoing momenta \mathbf{q}_i and outgoing momenta \mathbf{p}_j write a delta function $\delta^{(D)}\left(\sum_i \mathbf{q}_i - \sum_j \mathbf{p}_j\right)$
 - ii.) Assign a linear power spectrum $(2\pi)^3 \delta^{(D)}(\mathbf{q} + \mathbf{q}') P_{\text{lin}}(q)$ to each of the big circles with outgoing momenta \mathbf{q} and \mathbf{q}' . Divide by $\alpha(q)$ or $\alpha^2(q)$ for $P_{\delta\varphi}$ and $P_{\varphi\varphi}$, respectively.
 - iii.) For the outer fields with momenta \mathbf{k}_i write a delta function $\delta^{(D)}(\sum_i \mathbf{k}_i)$
 - iv.) For each square shaped vertex F_n with ingoing momenta \mathbf{q}_i write a mode coupling kernel $F_n(\mathbf{q}_1, \dots, \mathbf{q}_n)$
 - v.) For each triangular shaped vertex write a bias factor b_{ij}
 - vi.) For each diamond shaped vertex $G_{\text{NL}} = \{e_{\text{NL}}, f_{\text{NL}}, g_{\text{NL}}, \dots\}$ with outgoing momentum \mathbf{q} write $\alpha(\mathbf{q}) G_{\text{NL}}$
 - vii.) Integrate over all inner momenta $\int d^3 q_i / (2\pi)^3$
 - viii.) Multiply with the symmetry factor
 - ix.) Sum over all distinct labelings of the external lines
2. Add up the resulting expressions from all diagrams

4.5 Matter Power Spectrum

As a first application of our diagrammatic approach we write down the terms contributing to the non-Gaussian matter power spectrum and show the corresponding diagrams in Fig. 7

$$\begin{aligned}
P_{\text{mm}}(k) = & P_0(k) + P_{22}(k) + P_{13}(k) \\
& + \left(2\alpha^2(k) f_{\text{NL}}^2 \int \frac{d^3 q}{(2\pi)^3} \frac{P(q)}{\alpha^2(q)} \frac{P(\mathbf{k}-\mathbf{q})}{\alpha^2(\mathbf{k}-\mathbf{q})} \right)_A \\
& + \left(4\alpha(k) f_{\text{NL}} \int \frac{d^3 q}{(2\pi)^3} \frac{P(q)}{\alpha(q)} \frac{P(\mathbf{k}-\mathbf{q})}{\alpha(\mathbf{k}-\mathbf{q})} F_2(\mathbf{q}, \mathbf{k}-\mathbf{q}) \right)_B \\
& + \left(8f_{\text{NL}} \frac{P(k)}{\alpha(k)} \int \frac{d^3 q}{(2\pi)^3} \frac{P(q)}{\alpha(q)} F_2(\mathbf{q}, \mathbf{k}-\mathbf{q}) \alpha(\mathbf{k}-\mathbf{q}) \right)_C \\
& + \left(6\alpha(k) g_{\text{NL}} \frac{P(k)}{\alpha(k)} \int \frac{d^3 q}{(2\pi)^3} \frac{P(q)}{\alpha^2(q)} \right)_D,
\end{aligned} \tag{4.11}$$

where P_{13} and P_{22} are the standard one-loop corrections to the power spectrum (see [44] and Appendix A). The subscripts on the brackets in the above equation can be used to identify the corresponding terms in Fig. 7. The functional form agrees with previous results as presented in [53], who also performed a numerical evaluation which is thus not repeated here. The corrections arising from the f_{NL} terms are generally small and most prominent for high k , where the validity of perturbation theory has to be doubted.

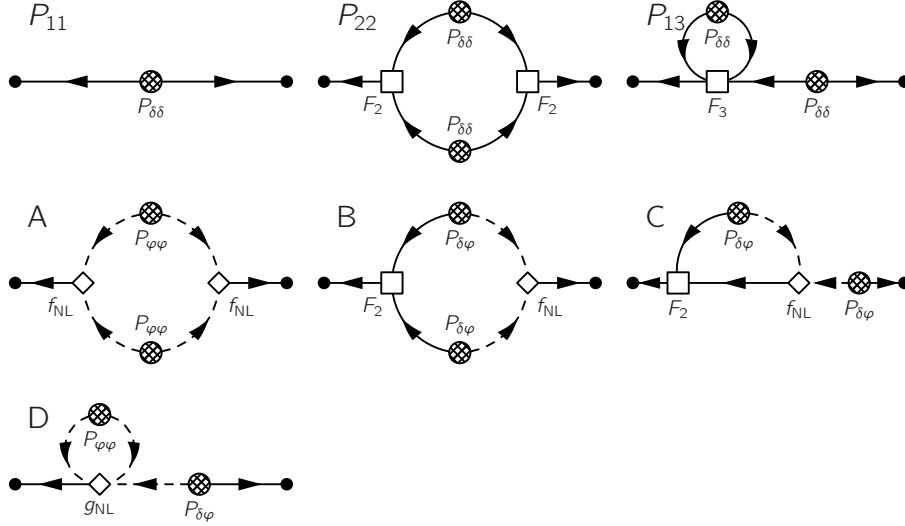


Figure 7. Diagrams contributing to the matter power spectrum as calculated in Eq. (4.11). The first line shows the standard PT terms, whereas the terms in the second and third line are purely non-Gaussian.

4.6 Matter Bispectrum

A non-vanishing matter bispectrum beyond the non-linear gravitational contribution would be a direct sign of non-Gaussian initial conditions. From the diagrams depicted in Fig. 8 we can derive the following expression for the tree-level matter bispectrum

$$B_{\text{mmm}}(\mathbf{k}_1, \mathbf{k}_2, \mathbf{k}_3) = \left(2P(k_1)P(k_2)F_2(\mathbf{k}_1, \mathbf{k}_2) + 2 \text{ cyc.} \right) + \left(2f_{\text{NL}} \frac{P(k_1)P(k_2)\alpha(k_3)}{\alpha(k_1)\alpha(k_2)} + 2 \text{ cyc.} \right) \tag{4.12}$$

$$= B_{F_2}(\mathbf{k}_1, \mathbf{k}_2, \mathbf{k}_3) + B_{f_{\text{NL}}}(\mathbf{k}_1, \mathbf{k}_2, \mathbf{k}_3) \tag{4.13}$$

Here *cyc.* is used to symbolise that the function arguments in the preceding terms have to be cyclically permuted as $\{(k_1, k_2, k_3), (k_2, k_3, k_1), (k_3, k_1, k_2)\}$. An evaluation of the latter term and comparison to n -body simulations is provided in a recent study by [54]. They find that the inclusion of one-loop terms leads to a considerable improvement of the agreement between theory and simulation on scales exceeding $k = 0.1 \, h\text{Mpc}^{-1}$.

Estimating the bispectrum of the dark matter distribution is an evolved task even for the upcoming lensing surveys. Thus we will focus our attention on the bispectra of biased tracers such as galaxies in the next section.

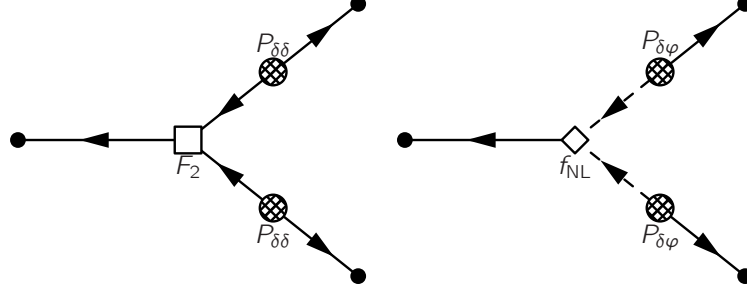


Figure 8. The two diagrams contributing to the tree level matter bispectrum B_{mmm} in Eq. (4.13).

5 Bispectra of Biased Tracers

In the following section we present the main result of this paper, the derivation of the halo bispectra. The bispectrum measures the correlation between three fields and thus halo and matter fields lead to four possible combinations. The matter auto-bispectrum was already discussed in the previous section such that we can focus our attention in this section to bispectra involving at least one biased tracer.

5.1 Halo Bispectrum

Summing up the diagrammatic expressions shown in Fig. 9 we can write down the tree-level expression for the halo auto-bispectrum

$$\begin{aligned}
B_{\text{hhh}}(\mathbf{k}_1, \mathbf{k}_2, \mathbf{k}_3) = & b_{10}^3 \left(2P(k_1)P(k_2)F_2(k_1, k_2) + 2f_{\text{NL}} \frac{P(k_1)P(k_2)\alpha(k_3)}{\alpha(k_1)\alpha(k_2)} + 2 \text{ cyc.} \right)_A \\
& + b_{10}^2 b_{01} \left(2P(k_1)P(k_2) \left(\frac{1}{\alpha(k_1)} + \frac{1}{\alpha(k_2)} \right) F_2(k_1, k_2) \right. \\
& + 2f_{\text{NL}} \frac{P(k_1)P(k_2)\alpha(k_3)}{\alpha(k_1)\alpha(k_2)} \left(\frac{1}{\alpha(k_1)} + \frac{1}{\alpha(k_2)} \right) + 2 \text{ cyc.} \left. \right)_B \\
& + b_{10} b_{01}^2 \left(2 \frac{P(k_1)P(k_2)}{\alpha(k_1)\alpha(k_2)} F_2(k_1, k_2) + 2f_{\text{NL}} \frac{P(k_1)P(k_2)\alpha(k_3)}{\alpha^2(k_1)\alpha^2(k_2)} + 2 \text{ cyc.} \right)_C \\
& + b_{01}^2 b_{02} \left(2 \frac{P(k_1)P(k_2)}{\alpha^2(k_1)\alpha^2(k_2)} + 2 \text{ cyc.} \right)_D \\
& + b_{01} b_{10} b_{02} \left(2 \frac{P(k_1)P(k_2)}{\alpha(k_1)\alpha(k_2)} \left(\frac{1}{\alpha(k_1)} + \frac{1}{\alpha(k_2)} \right) + 2 \text{ cyc.} \right)_E \\
& + b_{10}^2 b_{02} \left(2 \frac{P(k_1)P(k_2)}{\alpha(k_1)\alpha(k_2)} + 2 \text{ cyc.} \right)_F \\
& + b_{01}^2 b_{11} \left(\frac{P(k_1)P(k_2)}{\alpha(k_1)\alpha(k_2)} \left(\frac{1}{\alpha(k_1)} + \frac{1}{\alpha(k_2)} \right) + 2 \text{ cyc.} \right)_G
\end{aligned} \tag{5.1}$$

$$\begin{aligned}
& +b_{01}b_{10}b_{11} \left(P(k_1)P(k_2) \left(\frac{1}{\alpha^2(k_1)} + \frac{2}{\alpha(k_1)\alpha(k_2)} + \frac{1}{\alpha^2(k_2)} \right) + 2 \text{ cyc.} \right)_{\text{H}} \\
& +b_{10}^2b_{11} \left(P(k_1)P(k_2) \left(\frac{1}{\alpha(k_1)} + \frac{1}{\alpha(k_2)} \right) + 2 \text{ cyc.} \right)_{\text{I}} \\
& +b_{01}^2b_{20} \left(2\frac{P(k_1)P(k_2)}{\alpha(k_1)\alpha(k_2)} + 2 \text{ cyc.} \right)_{\text{J}} \\
& +b_{01}b_{10}b_{20} \left(2P(k_1)P(k_2) \left(\frac{1}{\alpha(k_1)} + \frac{1}{\alpha(k_2)} \right) + 2 \text{ cyc.} \right)_{\text{K}} \\
& +b_{10}^2b_{20} (2P(k_1)P(k_2) + 2 \text{ cyc.})_{\text{L}}
\end{aligned}$$

The subscripts on the brackets can be used to identify the terms with the corresponding diagrams in Fig. 9. Note that for $g_{\text{NL}} = 0$ the bias factors scale approximately as $b_{01} \propto f_{\text{NL}}$, $b_{02} \propto f_{\text{NL}}^2$ and $b_{11} \propto f_{\text{NL}}$. Thus the exponent of f_{NL} in the terms is the same as the exponent of $\alpha(k)$ in the denominator. Hence, it is the ratio of $f_{\text{NL}}/\alpha(k)$, where $k = \min\{k_1, k_2, k_3\}$ that is dominating the overall amplitude on large scales. The highest order contribution is f_{NL}^4 in the D term. This term is negative and gains importance for extremely small k and large f_{NL} .

The wave vectors are related by $\mathbf{k}_1 + \mathbf{k}_2 + \mathbf{k}_3 = 0$ and thus the configuration is fully determined by the magnitude of one vector k_1 , one angle $\mu = \mathbf{k}_1 \cdot \mathbf{k}_2 / (k_1 k_2)$ and the ratio of two vectors $x_2 = k_2/k_1$. The magnitude of the third vector is then given by

$$x_3 = \frac{k_3}{k_1} = \sqrt{1 + 2\mu x_2 + x_2^2}, \quad (5.2)$$

which for the isosceles configuration $k_1 = k_2$ simplifies to $x_3 = \sqrt{2(1 + \mu)}$. The transfer function is unity for large scale modes entering horizon after matter radiation equality and is damped on small scales, leading to an asymptotic slope of ≈ -1.75 . Starting from a primordial power spectrum $P_0(k) = Ak^n$ with $n \approx 1$ we see that the primordial Gaussian potential is scale invariant with $P_{\varphi\varphi} \propto k^{-3}$. The matter power spectrum in contrast is given by $P_{\delta\delta} = T^2(k)P_0(k)$ and thus it scales as k^1 at low k 's and approximately as $k^{-2.5}$ at high k 's. For the isosceles configuration and for low $k = k_1 = k_2$ the dominant contribution to terms including second order bias (terms D-L of the above equation) scales as

$$\frac{P(k_1)P(k_3)}{\alpha^i(k_1)\alpha^j(k_3)} \propto \frac{k^2 x_3}{k^{2i+2j} x_3^{2j}} = k^{2-2i-2j} x_3^{1-2j}, \quad (5.3)$$

while the dominant contribution to the A, B, C terms scales as

$$\frac{P(k_1)P(k_3)}{\alpha^{i-1}(k_1)\alpha^j(k_3)} \propto \frac{k^2 x_3}{k^{2i+2j-2} x_3^{2j}} = k^{4-2i-2j} x_3^{1-2j}. \quad (5.4)$$

The latter equation considers only the f_{NL} contribution, dominating at small x_3 's. In Table 1 we quote the exponents i, j and the corresponding power of f_{NL} . The combination $2(i + j - 1)$ is the exponent of the dominating short mode in the squeezed limit and can go up to k^6 . The estimation of the importance of the terms is further complicated by the different bias prefactors. We thus evaluate the expression numerically and discuss the results in Sec. 5.3 below.

Recent studies of the tree-level bispectrum [55] are based on the univariate bias parameters b_{10} and b_{20} only (univariate or Gaussian biasing). At tree level they thus consider only a subset of the above terms (see their Eq. (18)) leading to

$$B_{\text{hhh}}(\mathbf{k}_1, \mathbf{k}_2, \mathbf{k}_3) = b_{10}^3 [B_{F_2}(\mathbf{k}_1, \mathbf{k}_2, \mathbf{k}_3) + B_{f_{\text{NL}}}(\mathbf{k}_1, \mathbf{k}_2, \mathbf{k}_3)] + b_{10}^2 b_{20} [2P(k_1)P(k_2) + 2 \text{ cyc.}], \quad (5.5)$$

where B_{F_2} and $B_{f_{\text{NL}}}$ are implicitly defined in Eq. (4.13). This approach neglects the influence of non-Gaussianity on the bias parameters, whereas it has been explicitly shown in simulations [15, 18, 27] that local non-Gaussianity introduces a scale dependent bias.

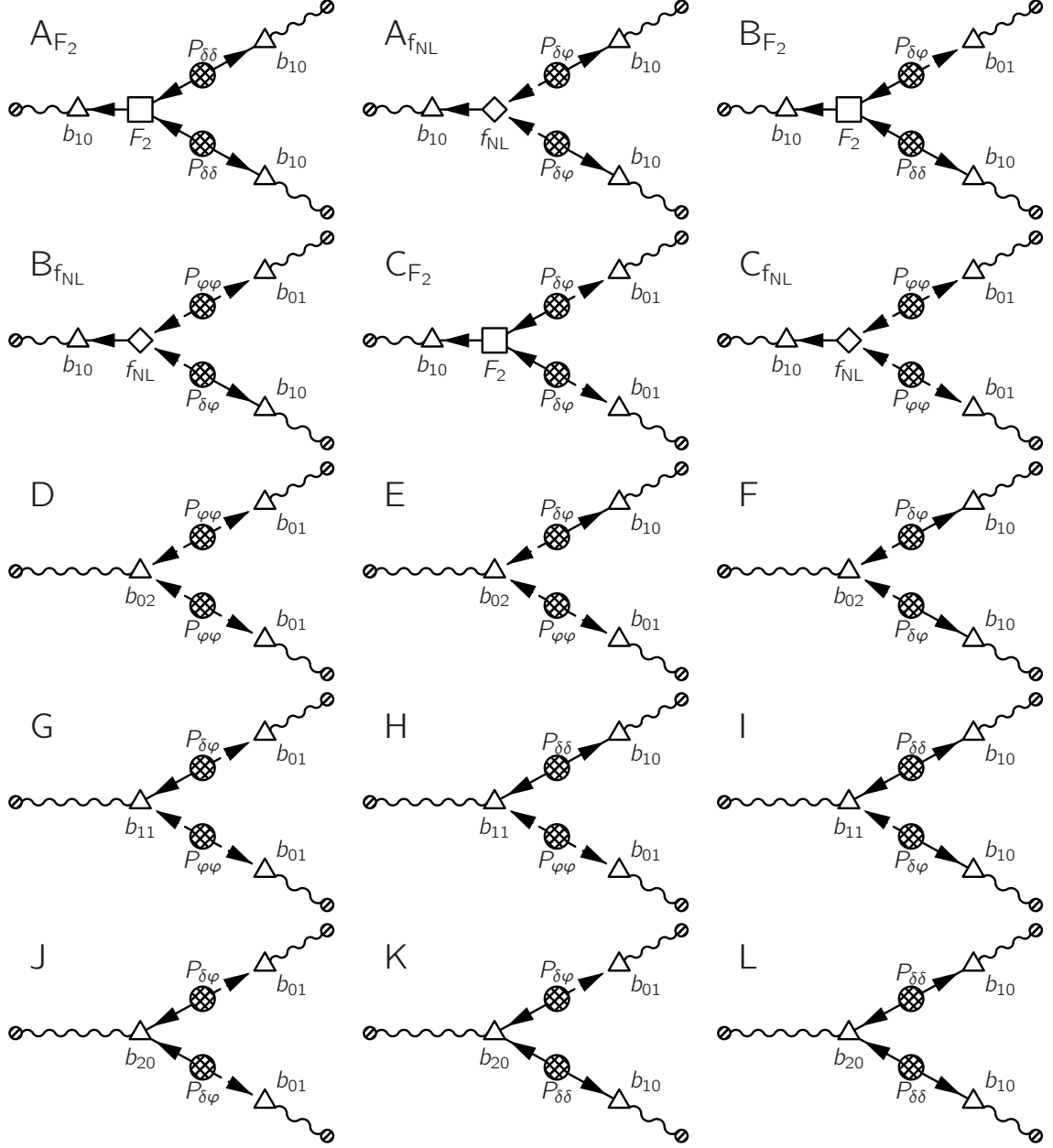


Figure 9. Tree level bispectrum diagrams considered for Eq. (5.1). The scaling of the different terms with f_{NL} as well as their k dependence are described in Table 1.

	i	j	$2(i+j-1)$	$2j-1$	f_{NL}
A_{F_2}	0	0	-2	-1	0
$A_{f_{\text{NL}}}$	1	1	2	1	1
B_{F_2}	0	1	0	1	1
$B_{f_{\text{NL}}}$	1	2	2	3	2
C_{F_2}	1	1	2	1	2
$C_{f_{\text{NL}}}$	2	2	6	3	3
D	2	2	6	3	4
E	2	1	4	1	3
	1	2	4	3	3
F	1	1	2	1	2
G	2	1	4	1	3
	1	2	4	3	3
H	2	0	2	-1	2
	1	1	2	1	2
	0	2	2	3	2
I	1	0	0	-1	1
	0	1	0	1	1
J	1	1	2	1	2
K	1	0	0	-1	1
	0	1	0	1	1
L	0	0	-2	-1	0

Table 1. Order of the terms contributing to the bispectrum B_{hhh} in Eq. (5.1) as defined via Eq. (5.3). From left to right we quote the exponents of the k -vectors, the exponent of the long k -mode, the exponent of the long-short ratio and the exponent of f_{NL} . More than one line per diagram can arise if there are different possibilities for combining the components of the diagram.

5.2 Cross-Bispectra

The measurement of the halo auto-bispectrum is limited by the finite number of haloes and shotnoise. Thus it is interesting to consider also the cross spectra between matter and haloes. Weak gravitational lensing in cross-correlation with galaxies could be a possible observational probe providing measurements of these effects. Without showing the diagrams we write down the expressions for the halo-halo-matter bispectrum:

$$\begin{aligned}
B_{\text{hhm}}(\mathbf{k}_1, \mathbf{k}_2, \mathbf{k}_3) = & b_{10}^2 \left(6F_2(\mathbf{k}_1, \mathbf{k}_2)P(k_1)P(k_2) + 6f_{\text{NL}}\alpha(k_3)\frac{P(k_1)}{\alpha(k_1)}\frac{P(k_2)}{\alpha(k_2)} + 2 \text{ cyc.} \right) \\
& + b_{01}b_{10} \left(4F_2(\mathbf{k}_1, \mathbf{k}_2)P(k_1)P(k_2) \left(\frac{1}{\alpha(k_1)} + \frac{1}{\alpha(k_2)} \right) \right. \\
& \left. + 4f_{\text{NL}}\alpha(k_3)P(k_1)P(k_2) \left(\frac{1}{\alpha^2(k_1)\alpha(k_2)} + \frac{1}{\alpha(k_1)\alpha^2(k_2)} \right) + 2 \text{ cyc.} \right) \\
& + b_{01}^2 \left(2F_2(\mathbf{k}_1, \mathbf{k}_2)\frac{P(k_1)P(k_2)}{\alpha(k_1)\alpha(k_2)} + 2f_{\text{NL}}\alpha(k_3)\frac{P(k_1)P(k_2)}{\alpha^2(k_1)\alpha^2(k_2)} + 2 \text{ cyc.} \right) \\
& + b_{10}b_{20} \left(4P(k_1)P(k_2) + 2 \text{ cyc.} \right) \\
& + b_{20}b_{01} \left(2P(k_1)P(k_2) \left(\frac{1}{\alpha(k_1)} + \frac{1}{\alpha(k_2)} \right) + 2 \text{ cyc.} \right) \\
& + b_{11}b_{10} \left(2P(k_1)P(k_2) \left(\frac{1}{\alpha(k_1)} + \frac{1}{\alpha(k_2)} \right) + 2 \text{ cyc.} \right) \\
& + b_{11}b_{01} \left(P(k_1)P(k_2) \left(\frac{1}{\alpha^2(k_1)} + \frac{2}{\alpha(k_1)\alpha(k_2)} + \frac{1}{\alpha^2(k_2)} \right) + 2 \text{ cyc.} \right) \\
& + b_{10}b_{02} \left(4\frac{P(k_1)P(k_2)}{\alpha^2(k_1)\alpha^2(k_2)} + 2 \text{ cyc.} \right)
\end{aligned} \tag{5.6}$$

$$+b_{02}b_{01}\left(2P(k_1)P(k_2)\left(\frac{1}{\alpha^2(k_1)\alpha(k_2)}+\frac{1}{\alpha(k_1)\alpha^2(k_2)}\right)+2\text{ cyc.}\right)$$

The corresponding prediction of a purely univariate bias model is given by

$$B_{\text{hbm}}(\mathbf{k}_1, \mathbf{k}_2, \mathbf{k}_3) = 3b_{10}^2 [B_{F_2}(\mathbf{k}_1, \mathbf{k}_2, \mathbf{k}_3) + B_{f_{\text{NL}}}(\mathbf{k}_1, \mathbf{k}_2, \mathbf{k}_3)] + 2b_{10}b_{20} [2P(k_1)P(k_2) + 2\text{ cyc.}]. \quad (5.7)$$

Finally, one can also correlate two matter and one halo density field:

$$\begin{aligned} B_{\text{hmm}}(\mathbf{k}_1, \mathbf{k}_2, \mathbf{k}_3) = & b_{10}\left(6F_2(\mathbf{k}_1, \mathbf{k}_2)P(k_1)P(k_2) + 6f_{\text{NL}}\alpha(k_3)\frac{P(k_1)P(k_2)}{\alpha(k_1)\alpha(k_2)} + 2\text{ cyc.}\right) \\ & + b_{01}\left(2F_2(\mathbf{k}_1, \mathbf{k}_2)P(k_1)P(k_2)\left(\frac{1}{\alpha(k_1)} + \frac{1}{\alpha(k_2)}\right) \right. \\ & \left. + 2f_{\text{NL}}P(k_1)P(k_2)\left(\frac{1}{\alpha^2(k_1)\alpha(k_2)} + \frac{1}{\alpha(k_1)\alpha^2(k_2)}\right) + 2\text{ cyc.}\right) \\ & + b_{20}\left(2P(k_1)P(k_2) + 2\text{ cyc.}\right) \\ & + b_{11}\left(P(k_1)P(k_2)\left(\frac{1}{\alpha(k_1)} + \frac{1}{\alpha(k_2)}\right) + 2\text{ cyc.}\right) \\ & + b_{02}\left(2\frac{P(k_1)P(k_2)}{\alpha(k_1)\alpha(k_2)} + 2\text{ cyc.}\right), \end{aligned} \quad (5.8)$$

where the corresponding prediction of the univariate bias model reads as

$$B_{\text{hmm}}(\mathbf{k}_1, \mathbf{k}_2, \mathbf{k}_3) = 3b_{10} [B_{F_2}(\mathbf{k}_1, \mathbf{k}_2, \mathbf{k}_3) + B_{f_{\text{NL}}}(\mathbf{k}_1, \mathbf{k}_2, \mathbf{k}_3)] + b_{20} [2P(k_1)P(k_2) + 2\text{ cyc.}]. \quad (5.9)$$

As for the halo auto-bispectrum, we show the results of a numerical evaluation of the above results in the next subsection.

5.3 Discussion of the Results

In this section we focus on the evaluation and discussion of the bispectrum expressions derived in Section 5 above. For the evaluation no smoothing is required since at tree level there are no integrations. The effect of smoothing at tree level breaks down to a multiplication with a smoothing function and thus suppresses the result on small scales keeping the large scales unaffected. The bias parameters are evaluated for a peak height of $\nu = 4$ corresponding to haloes of $M \approx 1 \times 10^{14} h^{-1} M_\odot$ and our fiducial cosmology introduced in Section 2.

In Fig. 10 we evaluate the terms in Eq. (5.1) separately to asses their importance. To make the comparison of the terms easier we plot the reduced bispectrum

$$Q(k_1, k_2, k_3) = \frac{B(k_1, k_2, k_3)}{P(k_1)P(k_2) + P(k_2)P(k_3) + P(k_3)P(k_1)}. \quad (5.10)$$

- We see that diagram A 's contribution is constant at high- k 's and grows at low- k 's. This is due to the fact that at high- k 's the signal from the subdiagram A_{F_2} grows (a fact that by the way Q is designed means that Q is constant), while on large scales the signal from the $A_{f_{\text{NL}}}$ grows. The two subdiagrams have a different scale dependence.
- It is easy to see that diagrams B are obtained by substituting δ -bias with the one in φ . Since φ is suppressed with respect to δ for high- k 's, we have that the signal in B is peaked at smaller k 's. The value of f_{NL} used for this plot is rather large, thus the B contribution is larger than the one of A at small k 's.
- In order to pass to the C diagrams, we exchange one δ leg with a φ leg and exchange a b_{10} factor with a b_{01} . Since in the B diagram one of the φ legs is already associated to the low k mode, we need to associate the remaining leg to a high k mode. This means that the C diagram scales

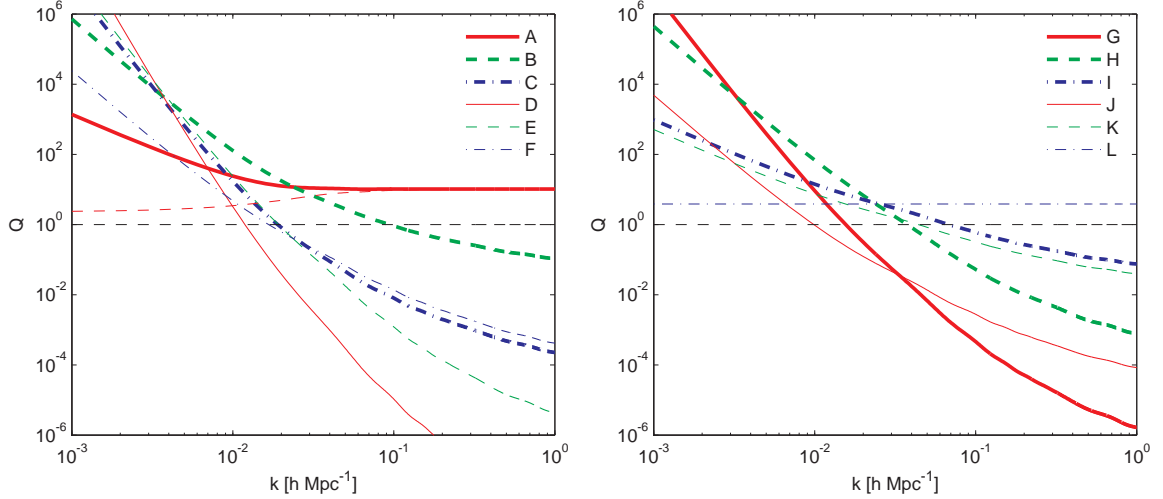


Figure 10. Scale dependence of the terms contributing to the halo bispectrum B_{hhh} in Eq. (5.1) for $f_{\text{NL}} = 100$ and $\nu = 4$ in an isosceles configuration $k = k_1 = k_2$, $\mu = -0.99$. The lines are labelled according to the corresponding diagrams in Fig. 9 and Table 1. The thin red dashed line in the left panel shows the bispectrum in the Gaussian case, which vanishes on large scales due to the shape dependence of the F_2 kernel. We show the reduced bispectrum defined in Eq. (5.10). The amplitude of the terms is determined both by the bias prefactors and the amplitude of the k -dependent factors. We see that the B and H terms are dominating on intermediate scales $k \approx 1 \times 10^{-2} \text{ hMpc}^{-1}$, whereas D, E and G take over on smaller k 's.

with respect to the B diagram by a factor of $b_{01}/(b_{10}\alpha(k_{\text{high}}))$ that, for the values of f_{NL} and k_{high} , that we are using is about a factor of 10 at the smallest k 's we plot. Notice that since the terms here have additional factors of $1/k^2$, it raises more steeply at low k 's. Even more than for the B diagram, this term becomes irrelevant at high k 's because of the many φ factors that it involves.

- The remaining diagrams $D - L$ are constructed using the non-linear biases in all possible contractions. This means that the steepest at low k 's will be the D diagram that involves b_{02} and b_{01}^2 , while the most important at high k 's will be the L diagram, that does not involve any φ . By construction the L diagram is scale independent when plotted in terms of its contribution to the reduced bispectrum Q .

In Fig. 11, we show how the various diagrams scale with the shape parameter x_3 in the isosceles configuration. For to overall size we consider $k = 0.1 \text{ hMpc}^{-1}$ and $k = 0.01 \text{ hMpc}^{-1}$. The x_3 scaling is also given in Table 1 and can be easily reconstructed from Eqs. (5.3) and (5.4). There is a clear correction at small k 's from the φ terms. Since the signal is not scale invariant, as we move to higher k 's, the contribution from terms involving δ_{m} and its non-linearities, such as the A_{F_2} diagram, gain importance.

The left panel of Fig. 12 shows the dependence of the bispectrum amplitude on the variation of the non-Gaussianity parameter f_{NL} . This plot shows that higher than linear powers in f_{NL} have to be considered to describe the full bispectrum amplitude. The plot also shows that the sensitivity to f_{NL} increases as one considers more squeezed configurations. While evaluated for a different halo sample and redshift, the plot shows qualitative agreement with the simulation measurements of [56]. In the right panel of Fig. 12 we plot the angular dependence of the bispectrum for an almost isosceles configuration $k_1 = k_2/1.2$ since the exact isosceles configuration is divergent for $\theta \rightarrow \pi$. Here $\theta = \arccos(\mu)$ refers to the angle between \mathbf{k}_1 and \mathbf{k}_2 .⁸ Besides an overall enhancement the most remarkable feature is the upturn of the multivariate bias prediction in the squeezed limit.

⁸The divergence of the isosceles case means nothing but the fact that as $\theta \rightarrow \pi$ one of the sides of the triangle goes to zero, and so the bispectrum amplitude goes formally to infinity.

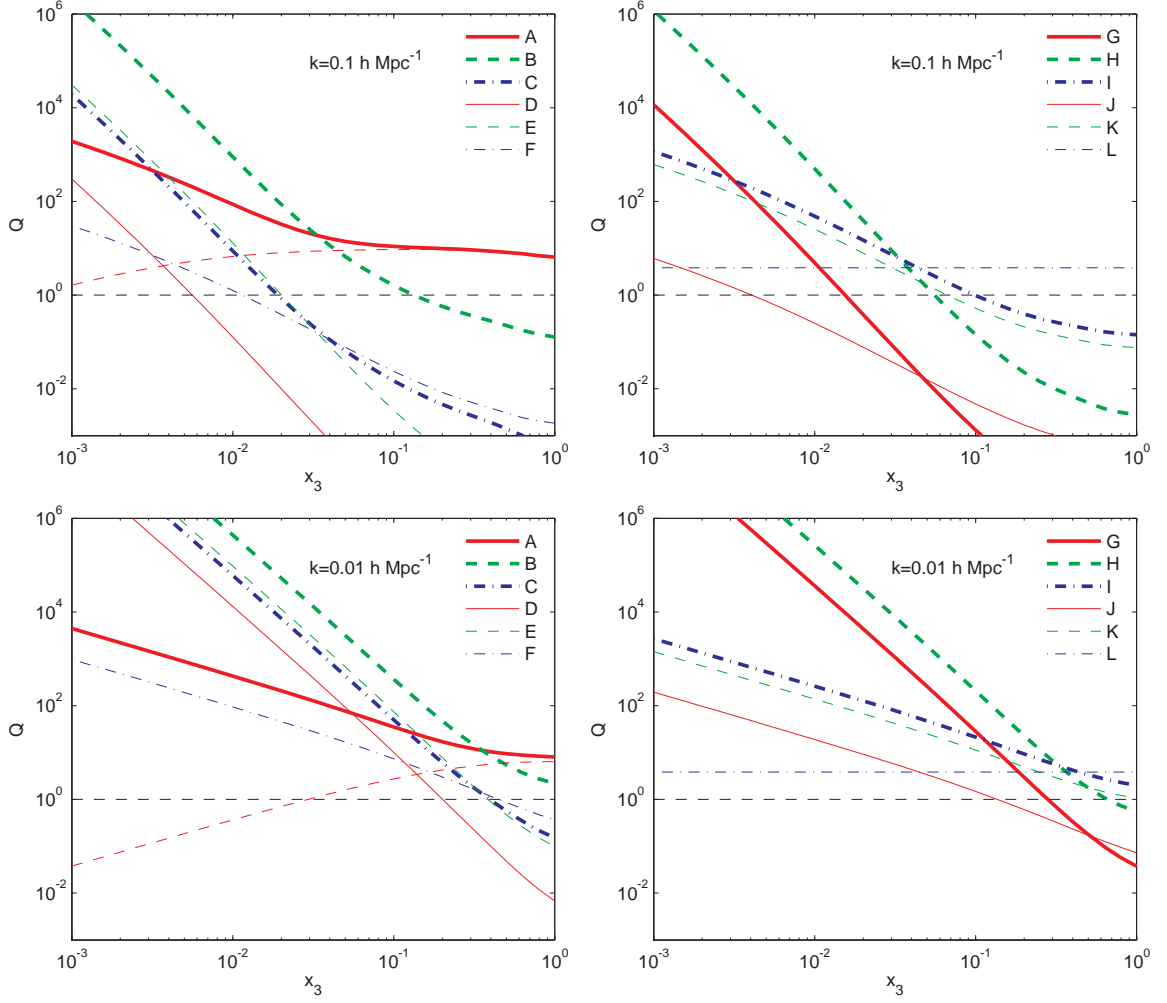


Figure 11. Dependence of the terms contributing to the halo bispectrum B_{hhh} in Eq. (5.1) on the long-short axis ratio x_3 for an isosceles configuration with $k = k_1 = k_2$. The overall scale of the triangle is $k = 0.1 \, h\text{Mpc}^{-1}$ for the upper panels and $0.01 \, h\text{Mpc}^{-1}$ for the lower panels. This plot clearly shows the effect of the φ -bias corrections in the squeezed limit $x_3 \rightarrow 0$. As in the above plot the thin red dashed line in the left panels shows the A_{F_2} contribution.

Fig. 13 shows the halo auto- and cross-bispectra. We show both their scale dependence as well as the ratio to the Gaussian expression for a squeezed isosceles configuration $k_1 = k_2, \mu = -0.99, x_3 \approx 1/7$ and compare to the predictions of the univariate bias model. These figures show that the non-Gaussian bispectrum asymptotes to the Gaussian one for high k 's (small scales). On larger scales both the univariate bias model as well as our prediction are increased with respect to the Gaussian case due to the coupling between long and short modes. Our expression for B_{hhh} predicts an enhancement by a factor of 2 with respect to the existing univariate biasing calculations on scales of $k \approx 0.03 \, h\text{Mpc}^{-1}$. The enhancement is less pronounced for the mixed halo-matter bispectra. From the scaling with k and x_3 in Eq. (5.3) and Table 1 it is clear that the bispectrum amplitude is largest for squeezed configurations $\mu \rightarrow -1, \theta \rightarrow \pi$ and low overall scale $k \rightarrow 0$. However, the shape and scale of the triangle are limited by the fundamental mode and the sampling variance in exactly this limit. We will quantify the signal-to-noise ratio in the next section.

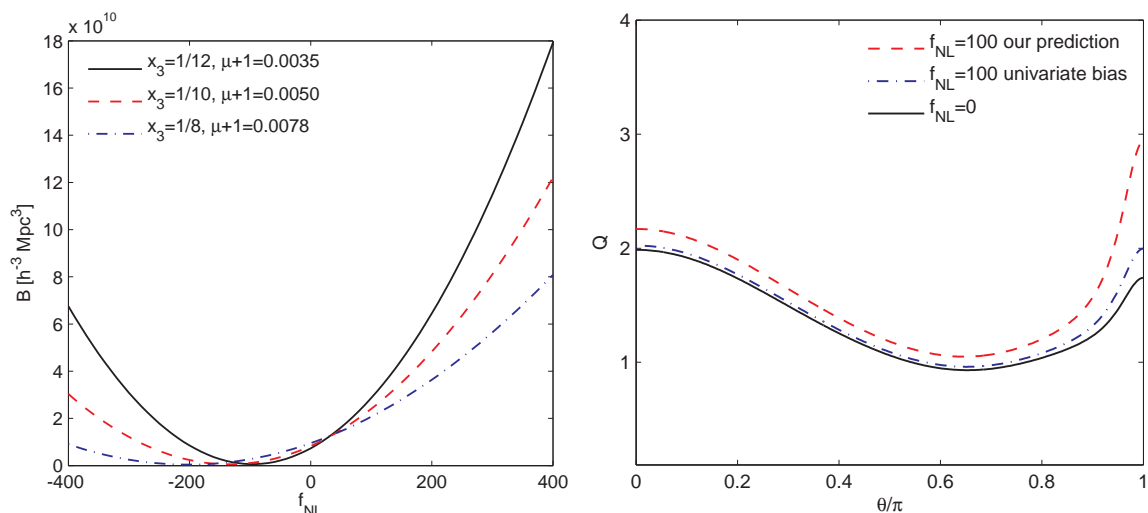


Figure 12. *Left panel:* Dependence of the amplitude of the halo bispectrum B_{hhh} on the non-Gaussianity parameter f_{NL} for $g_{\text{NL}} = 0$ and $k_1 = k_2 = 0.042 \, h\text{Mpc}^{-1}$. We show the bispectrum amplitude for three different values of the short-long ratio x_3 defined in Eq. (5.2). This plot agrees qualitatively with Fig. 4 in [56]. It is obvious from this plot that the bispectrum decreases with respect to the Gaussian non-linear clustering case for weakly negative f_{NL} . *Right panel:* Angular dependence of the non-Gaussian and Gaussian reduced bispectra for $f_{\text{NL}} = 100$ as a function of $\theta = \arccos(\mathbf{k}_1, \mathbf{k}_2) = \arccos(\mu)$ for a halo sample with $\nu = 4$ and a nearly isosceles configuration with $k_1 = k_2/1.2 = 0.03 \, h\text{Mpc}^{-1}$. We show our result (5.1) (red dashed) and the univariate biasing result (5.5) (blue dash-dotted). Besides the overall enhancement of the multivariate bias result with respect to the univariate bias result there is a remarkable upturn for $\theta \rightarrow \pi$.

5.4 Comparison to Simulations

While a full simulation based analysis of the halo bispectrum goes beyond the scope of this paper, we can nevertheless compare to published simulation measurements. The only published simulation measurement of the halo bispectrum we are aware of, was performed on a $L = 2000 \, h^{-1}\text{Mpc}$ cosmological simulation by [56]. They consider a cosmology with $\sigma_8 = 0.816$, $\Omega_{\text{m}} = 0.28$, $\Omega_{\Lambda} = 0.72$ and present their results for $z = 0.5$. In Fig. 14 we show the comparison between our theoretical predictions and their simulation measurement for a halo sample with $M > 4.6 \times 10^{13} \, h^{-1}M_{\odot}$. The bias value inferred from the simulations $b_{10,\text{sim}} = 2.9$ [57] points towards a halo sample with $M > 7 \times 10^{13} \, h^{-1}M_{\odot}$. This deviation to the low mass cutoff quoted by the authors might be due to an incomplete sampling of haloes around the cutoff. We adopt $M > 7 \times 10^{13} \, h^{-1}M_{\odot}$ as the lower boundary of the halo sample and calculate the average bias parameters using the LV mass function. Consistent with [56] we rescale b_{01} as $b_{01} \rightarrow 0.75 \, b_{01}$, a modification motivated by ellipsoidal collapse (although this seems to apply only to Friends-of-friends identified halos and not to spherical overdensity halos, [2]). Fig. 14 shows that the scale and shape dependence is quite well described by the theory, especially the upturn of the bispectrum for squeezed configurations. The disagreement between our predictions and the simulation measurement on scales of $k \approx 0.1 \, h\text{Mpc}^{-1}$ is probably due to loop corrections in the matter bispectrum [54] or to the inaccuracy of the non-Gaussian mass function that we have used to extract the bias parameters.⁹

⁹It is indeed possible that other non-Gaussian mass functions might give improved results, but a more careful treatment of these effects goes beyond the scope of our paper.

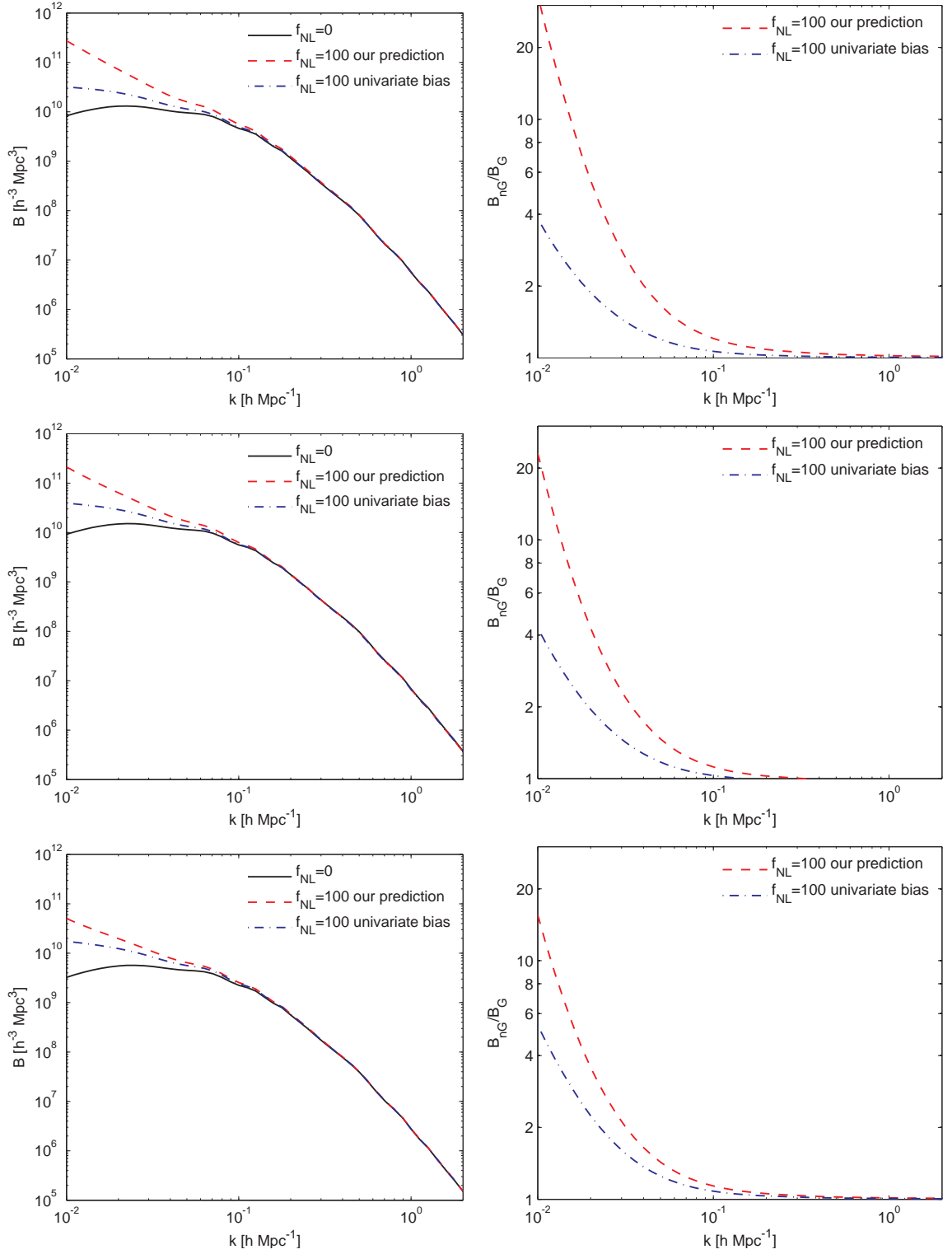


Figure 13. *Upper Left Panel:* Halo auto bispectrum B_{hhh} according to Eq. (5.1) for $f_{\text{NL}} = 100$ and $\mu = -0.99$. We show the Gaussian bispectrum (black solid line), the univariate bias prediction of Eq. (5.5) (blue dash dotted) and our predictions (red dashed). *Upper Right panel:* Ratio of the non-Gaussian bispectra and the Gaussian bispectrum shown in the left panel. *Middle Panels:* Same as above, but for the halo-matter cross bispectrum B_{hhm} according to Eq. (5.6). *Lower Panels:* Same as above, but for the halo-matter cross bispectrum B_{hmm} according to Eq. (5.8).

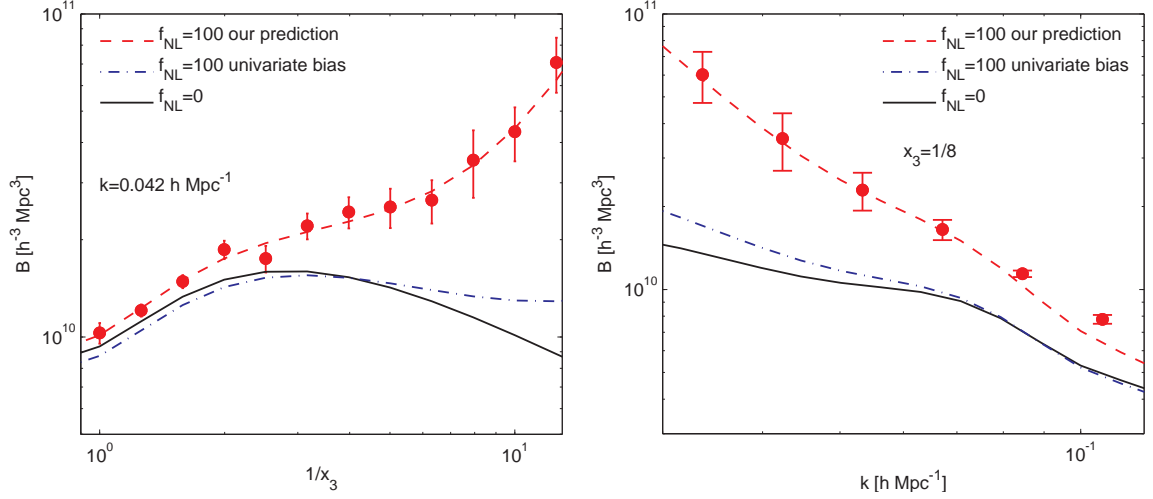


Figure 14. Halo bispectrum in the isosceles configuration $k_1 = k_2$ for $z = 0.5$ and $M > 4.6 \times 10^{13} h^{-1} M_\odot$ in comparison to the data points in Fig. (6) of [56]. The lines show the multivariate bias (red dashed) and univariate bias (blue dash-dotted) non-Gaussian bispectrum as well as the Gaussian bispectrum (black solid). We adjust the low mass cutoff to bring the bias parameters derived from the mass function in agreement with the simulation measurement $b_{10} = 2.9$ and rescale $b_{01} \rightarrow 0.75 b_{01}$. *Left panel:* Bispectrum as a function of the high-low- k ratio $1/x_3 = k/k_3$ and $k = 0.042 h\text{Mpc}^{-1}$. *Right panel:* Bispectrum as a function of scale k for $1/x_3 = 7.94$.

6 Signal-to-Noise

One goal of this work is to show the viability of the bispectrum to put constraints on primordial non-Gaussianity. The question is whether it is worth the additional effort of measuring the halo bispectrum given that the halo power spectrum can be used to put constraints on non-Gaussianity as well. The bispectrum analysis is clearly naively more sensitive than the power spectrum to non-Gaussianities but it remains to show that this can overcome the enhanced errors. To estimate the errors we assume a survey of volume V from which the halo density field $\delta_h(\mathbf{k})$ is estimated. The bispectrum and power spectrum estimators are constructed from a decomposition of k -space into spherical shells of width δk . Then the k -modes within the shell are spherically averaged to obtain the estimators [58]

$$\hat{P}(k) = \frac{V_f}{V_{12}} \int_k \frac{d^3 q_1}{(2\pi)^3} \int_k \frac{d^3 q_2}{(2\pi)^3} \delta(\mathbf{q}_1) \delta(\mathbf{q}_2) \delta^{(D)}(\mathbf{q}_1 + \mathbf{q}_2) \quad (6.1)$$

for the power spectrum and

$$\hat{B}(\mathbf{k}_1, \mathbf{k}_2, \mathbf{k}_3) = \frac{V_f}{V_{123}} \int_{k_1} \frac{d^3 q_1}{(2\pi)^3} \int_{k_2} \frac{d^3 q_2}{(2\pi)^3} \int_{k_3} \frac{d^3 q_3}{(2\pi)^3} \delta(\mathbf{q}_1) \delta(\mathbf{q}_2) \delta(\mathbf{q}_3) \delta^{(D)}(\mathbf{q}_1 + \mathbf{q}_2 + \mathbf{q}_3) \quad (6.2)$$

for the bispectrum, where the integrals are over spherical shells $q_i \in [k_i - \delta k/2, k_i + \delta k/2]$. As shown in [58] the covariance of this bispectrum estimator is given by

$$(\Delta B)^2 = s_{123} \frac{V_f}{V_{123}} \left(P_h(k_1) + \frac{1}{\bar{n}} \right) \left(P_h(k_2) + \frac{1}{\bar{n}} \right) \left(P_h(k_3) + \frac{1}{\bar{n}} \right) \quad (6.3)$$

and the one for the power spectrum [58, 59] by

$$(\Delta P)^2 = 2 \frac{V_f}{V_{12}} \left(P_h(k_1) + \frac{1}{\bar{n}} \right) \left(P_h(k_2) + \frac{1}{\bar{n}} \right). \quad (6.4)$$

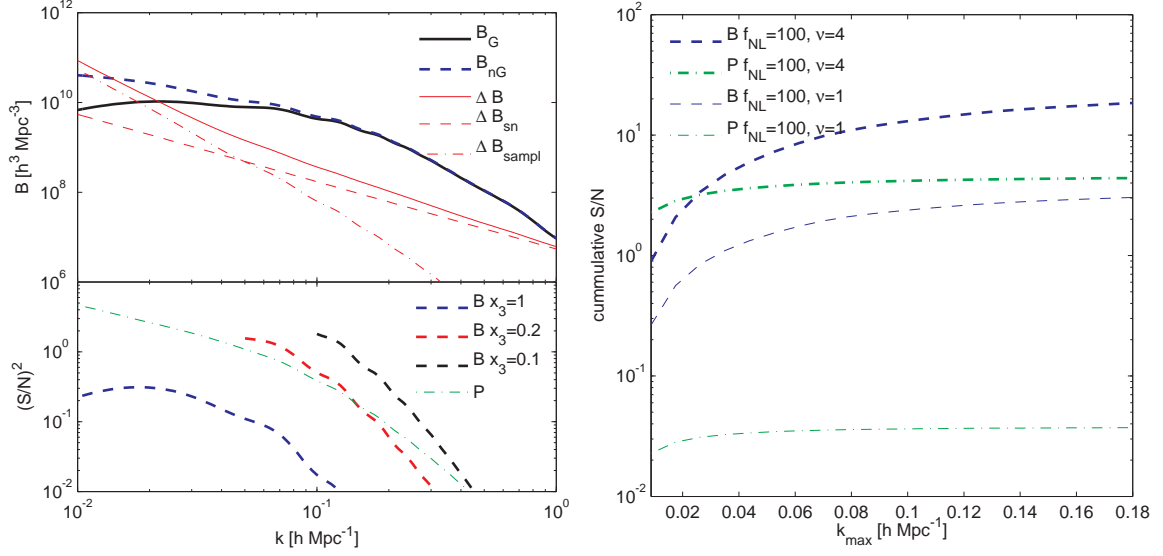


Figure 15. *Left top panel:* Variance of the halo bispectrum B_{hhh} for $f_{\text{NL}} = 100$, $x_3 = 0.1$. Gaussian (thick black) and non-Gaussian (thick blue dashed) bispectrum amplitude and error on the bispectrum for $\bar{n} = 1 \times 10^{-5} h^3 \text{Mpc}^{-3}$, $V = 10 h^{-3} \text{Gpc}^3$, $k_{\text{f}} = 2.9 \times 10^{-3} h \text{Mpc}^{-1}$ and $\delta k = 3k_{\text{f}} = 0.008 h \text{Mpc}^{-1}$. For the biased tracer we assume a halo sample with $\nu = 4$, corresponding to $M \approx 1 \times 10^{14} h^{-1} M_{\odot}$ ($b_{10} = 2.23$, $b_{20} = 0.38$). We plot the full error $\Delta B(k)$ (red) as well as the sampling variance (red dash-dotted) and shotnoise (red dashed) contributions. *Left bottom panel:* SNR for the halo bispectrum B_{hhh} (blue, red and green dashed for $x_3 = 1, 0.2$ and 0.1 from bottom to top) and the halo power spectrum P_{hh} (green dash-dotted). The signal is defined as the difference between the non-Gaussian and Gaussian prediction. As we go to higher k more squeezed configurations gain importance. *Right panel:* Cumulative signal-to-noise for the bispectrum (blue dashed) and power spectrum (green dash-dotted). We evaluate the SNR for $\nu = 4$ (thick) and $\nu = 1$ (thin).

Here s_{123} is a symmetry factor, with $s_{123} = 6, 2, 1$ for equilateral, isosceles and general configurations, respectively. In the noise estimators we approximate the halo power spectrum by the leading contribution $P_{\text{h}}(k) = (b_{10} + b_{01}/\alpha(k)) P_{\text{lin}}(k)$ for simplicity. The k -space volume of the fundamental cell is $V_{\text{f}} = k_{\text{f}}^3 = (2\pi)^3/L^3$ and the norm volumes are given by

$$V_{123} = \int_{k_1} \frac{d^3 q_1}{(2\pi)^3} \int_{k_2} \frac{d^3 q_2}{(2\pi)^3} \int_{k_3} \frac{d^3 q_3}{(2\pi)^3} \delta^{(\text{D})}(\mathbf{q}_{123}) \approx 8\pi^2 k_1 k_2 k_3 \delta k^3 \quad (6.5)$$

and

$$V_{12} = \int_{k_1} \frac{d^3 q_1}{(2\pi)^3} \int_{k_2} \frac{d^3 q_2}{(2\pi)^3} \delta^{(\text{D})}(\mathbf{q}_{12}) \approx 4\pi k_1 k_2 \delta k. \quad (6.6)$$

If $P \gg 1/\bar{n}$ the cosmic variance dominates whereas shotnoise dominates when $P \ll 1/\bar{n}$.

As our fiducial case we consider a survey of $V = 10 h^{-3} \text{Gpc}^3$ and $\delta k = 3k_{\text{f}} = 9 \times 10^{-3} h \text{Mpc}^{-1}$ and a halo sample with overdensity $\nu = 4$ corresponding to $M \approx 1 \times 10^{14} h^{-1} M_{\odot}$ ($b_{10} = 2.23$, $b_{20} = 0.38$). The number density of the halo sample is assumed to be $\bar{n} = 1 \times 10^{-5} h \text{Mpc}^{-3}$. The left top panel of Fig. 15 shows the errors and the signal-to-noise ratio (SNR) for the halo bispectrum B_{hhh} in a squeezed isosceles configuration $k = k_1 = k_2$, $x_3 = 0.1$. Here we define the signal as the signal-to-noise weighted difference between the total non-Gaussian and the fiducial Gaussian bispectrum amplitude

$$\text{SNR}_B^2(k_i, k_j, k_l) = \frac{(B_{\text{nG}}(k_i, k_j, k_l) - B_{\text{G}}(k_i, k_j, k_l))^2}{(\Delta B)^2(k_i, k_j, k_l)} \quad (6.7)$$

with an equivalent expression for the power spectrum. We see that the f_{NL} contribution enhances the signal on a wide range of scales and most relevantly on the smallest k 's. The left bottom panel of Fig. 15 shows the SNR for a given bin of k modes, for isosceles triangles with three different values of

x_3 . We see that the bispectrum signal is enhanced as we make the triangle more and more squeezed and as we take the highest k 's of the triangle closer to the non-linear scale. We should stress that our tree-level calculation does not apply for k 's close or larger than the non-linear scale. We finally also plot the binned SNR from the power spectrum, which is peaked at the smallest k 's. So far we restricted our discussion to a particular bispectrum configuration. For the extraction of a non-Gaussian signal from a survey one would rather add up all the possible information, *i. e.* sum over all possible configurations up to a maximum wavenumber k_{\max} . The total signal-to-noise is given by a sum over all the possible combinations of shells up to the maximum wavenumber k_{\max}

$$\left(\frac{S}{N}\right)_{\text{tot},B}^2 = \sum_{i=1}^{i_{\max}} \sum_{j=1}^i \sum_{l=i-j}^{i+j} \text{SNR}_B^2(k_i, k_j, k_l) \quad (6.8)$$

where we used $k_i = i\delta k$. In the right panel of Fig. 15 we plot the cumulative signal-to-noise for the bispectrum and power spectrum for $f_{\text{NL}} = 100$ and tracers with peak height $\nu = 4$ and $\nu = 1$. For the high bias tracer we see that for the considered survey and going up to $k_{\max} = 0.18 \text{ hMpc}^{-1}$ we could constrain $\sigma_{f_{\text{NL}}} \approx 5$ from the bispectrum analysis, whereas the power spectrum leads to constraints of $\sigma_{f_{\text{NL}}} \approx 25$. Note that we are plotting the total non-Gaussian signal. To obtain the SNR on f_{NL} , the lines in the figure have to be divided by f_{NL} . For k higher than about 0.1 hMpc^{-1} non-linear corrections should be implemented. The bispectrum wins over the power spectrum even if the maximum wave number is restricted to $k_{\max} \approx 0.03 \text{ hMpc}^{-1}$. Furthermore the plot shows that extraction of $f_{\text{NL}} = \mathcal{O}(10)$ is possible only with the bispectrum analysis but not with the power spectrum analysis for these tracers. Note that the choice of bias, volume and number density is similar to values for luminous red galaxies expected in SDSS-III (BOSS) redshift survey [60]. The bispectrum of the low bias $\nu = 1$ tracers shows an even more remarkable improvement in SNR compared to the corresponding power spectrum.

7 Conclusions

In this paper we present a diagrammatic prescription for the calculation of multipoint statistics of biased tracers of the cosmological density field accounting for the effect of non-Gaussian initial fluctuations. The diagrammatic approach combines biasing, non-Gaussianity and non-linear clustering into one consistent and intuitive picture. While we focused on the bispectrum, the generalisation to higher order correlators should be straightforward. Also, non-local shapes can be implemented using their primordial bispectrum instead of the mode coupling vertices in Fig. 6.

We use this diagrammatic prescription to derive the halo bispectrum accounting for all tree level/zero loop contributions. Unsurprisingly, the bispectrum is largest in the squeezed limit $x_3 \rightarrow 0$, where our prediction exceeds the results obtained using univariate bias only, by about a factor of 2 on scales of $k \approx 0.03 \text{ hMpc}^{-1}$. Given the fact, that we see these corrections compared to the univariate bias approach already at tree level, we caution the use of the univariate bias expansion as presented in [61] and [47]. While the qualitative results are quite general, the quantitative results presented in Section 5.3 are somewhat dependent on the choice of the halo sample. We considered a $\nu = 4$ tracer, corresponding to haloes of mass $M \approx 1 \times 10^{14} h^{-1} M_{\odot}$ ($b_{10} = 2.23$, $b_{20} = 0.38$).

Probably the most important result of this paper is that the halo bispectrum analysis offers an alternative to the power spectrum for detecting local non-Gaussianities with an even higher constraining power. For the $\nu = 4$ tracers in a $V = 10 \text{ h}^{-3} \text{ Gpc}^3$ survey, our signal-to-noise analysis predicts a factor of five improvement in the constraints on f_{NL} compared to the power spectrum. For lower bias tracers at the same number density the total signal-to-noise is a bit lower, but it is in fact much higher relative to the power spectrum analysis, which contains no signal for unbiased tracers.

Our results suggest that the bispectrum should be the statistic of choice for detecting primordial non-Gaussianity in current and future survey data. However, some additional work has to be done before this method can be applied to the real data. One extension is to make predictions for photometric surveys, where only projected density fluctuations are observed. Alternatively, if a redshift survey is used in the analysis then the predictions here should be generalized to include redshift space

distortions [62]. In the light of ever increasing surveys and simulations one might also be concerned about general relativistic corrections on horizon scales [31].

Convergence is probably one of the most important problems for perturbative calculations. For Gaussian initial conditions, comparisons of the matter bispectrum in simulations to the theoretical predictions as presented in [54] and [63] conclude that 1-loop calculations are required to achieve a reasonable agreement on scales of $k \approx 0.1 h^{-1}\text{Mpc}$. The bispectrum in presence of local non-Gaussianity is the perfect statistic to apply perturbation theory at tree level combined with the bias from the peak-background split since the non-Gaussian effects are most prominent for low k or large smoothing scales. Still, we focus on a tree level calculation and find that the signal receives relevant contributions from scales close to the non-linear scale. For this reason, loop-corrections should be examined to fully assess the detailed amplitude of the signal. As we discuss, this will probably require to study the cutoff dependence both of the loop corrections and of the bias coefficients, such that final observables do not depend on the cutoff.¹⁰ Some of these 1-loop terms will be renormalized and absorbed into the tree level terms discussed here. Still, a consistent calculation of the halo bispectrum at the next order would require consideration of non-linear couplings up to F_4 and biasing up to fourth order, both in δ and φ . This increases the number of terms by a large amount and goes beyond the scope of the current paper. The final decision about the validity of the perturbative calculation presented in this paper has to be based on a detailed comparison to the halo bispectrum measured in simulations. A first comparison of our results to the measurements published by [56] shows an encouraging level of agreement.

Acknowledgments

We acknowledge M. Zaldarriaga for initial collaboration on this project and for many discussions. Furthermore, we would like to thank N. Hamaus, P. McDonald, C. Porciani, F. Schmidt, R. Scoccimarro and in particular E. Sefusatti for helpful discussions. Special thanks to V. Desjacques both for fruitful discussions and comments on the manuscript. We would also like to thank T. Nishimichi for providing the data points of the simulation bispectrum measurement and the Asian Pacific Centre for Theoretical Physics in Pohang, Korea, for their kind hospitality during the workshop on "Cosmology and Fundamental Physics". This work is supported by DOE, the Swiss National Foundation under contract 200021-116696/1 and WCU grant R32-2009-000-10130-0.

References

- [1] M. Liguori, E. Sefusatti, J. R. Fergusson, and E. P. S. Shellard, *Primordial non-Gaussianity and Bispectrum Measurements in the Cosmic Microwave Background and Large-Scale Structure*, *ArXiv e-prints* (Jan., 2010) [[arXiv:1001.4707](#)].
- [2] V. Desjacques and U. Seljak, *Primordial non-Gaussianity from the large scale structure*, *ArXiv e-prints* (Mar., 2010) [[arXiv:1003.5020](#)].
- [3] A. H. Guth, *Inflationary universe: A possible solution to the horizon and flatness problems*, *Phys. Rev.* **23** (Jan., 1981) 347–356.
- [4] A. D. Linde, *A new inflationary universe scenario: A possible solution of the horizon, flatness, homogeneity, isotropy and primordial monopole problems*, *Physics Letters B* **108** (Feb., 1982) 389–393.
- [5] A. Albrecht and P. J. Steinhardt, *Cosmology for grand unified theories with radiatively induced symmetry breaking*, *Physical Review Letters* **48** (Apr., 1982) 1220–1223.
- [6] C. Cheung, A. L. Fitzpatrick, J. Kaplan, L. Senatore, and P. Creminelli, *The effective field theory of inflation*, *Journal of High Energy Physics* **3** (Mar., 2008) 14–014, [[arXiv:0709.0293](#)].
- [7] E. Komatsu, K. M. Smith, J. Dunkley, C. L. Bennett, B. Gold, G. Hinshaw, N. Jarosik, D. Larson, M. R.olta, L. Page, D. N. Spergel, M. Halpern, R. S. Hill, A. Kogut, M. Limon, S. S. Meyer,

¹⁰ Previous studies [47, 61] did not stress the conceptual separation between the smoothing scale, the cutoff of the loops and the mass scale of the halos.

- N. Odegard, G. S. Tucker, J. L. Weiland, E. Wollack, and E. L. Wright, *Seven-Year Wilkinson Microwave Anisotropy Probe (WMAP) Observations: Cosmological Interpretation*, *ArXiv e-prints* (Jan., 2010) [[arXiv:1001.4538](#)].
- [8] E. Sefusatti and R. Scoccimarro, *Galaxy bias and halo-occupation numbers from large-scale clustering*, *Phys. Rev.* **71** (Mar., 2005) 063001–+, [[astro-ph/0412626](#)].
- [9] D. S. Salopek and J. R. Bond, *Nonlinear evolution of long-wavelength metric fluctuations in inflationary models*, *Phys. Rev.* **42** (Dec., 1990) 3936–3962.
- [10] D. S. Salopek and J. R. Bond, *Stochastic inflation and nonlinear gravity*, *Phys. Rev.* **43** (Feb., 1991) 1005–1031.
- [11] L. Senatore and M. Zaldarriaga, *The Effective Field Theory of Multifield Inflation*, *ArXiv e-prints* (Sept., 2010) [[arXiv:1009.2093](#)].
- [12] N. Dalal, O. Doré, D. Huterer, and A. Shirokov, *Imprints of primordial non-Gaussianities on large-scale structure: Scale-dependent bias and abundance of virialized objects*, *Phys. Rev.* **77** (June, 2008) 123514–+, [[arXiv:0710.4560](#)].
- [13] S. Matarrese and L. Verde, *The Effect of Primordial Non-Gaussianity on Halo Bias*, *Astrophys. J. Let.* **677** (Apr., 2008) L77–L80, [[arXiv:0801.4826](#)].
- [14] A. Slosar, C. Hirata, U. Seljak, S. Ho, and N. Padmanabhan, *Constraints on local primordial non-Gaussianity from large scale structure*, *Journal of Cosmology and Astro-Particle Physics* **8** (Aug., 2008) 31–+, [[arXiv:0805.3580](#)].
- [15] V. Desjacques, U. Seljak, and I. T. Iliev, *Scale-dependent bias induced by local non-Gaussianity: a comparison to N-body simulations*, *Mon. Not. Roy. Astron. Soc.* **396** (June, 2009) 85–96, [[arXiv:0811.2748](#)].
- [16] V. Desjacques and U. Seljak, *Signature of primordial non-Gaussianity of ϕ^3 -type in the mass function and bias of dark matter haloes*, *ArXiv e-prints* (July, 2009) [[arXiv:0907.2257](#)].
- [17] M. Grossi, K. Dolag, E. Branchini, S. Matarrese, and L. Moscardini, *Evolution of massive haloes in non-Gaussian scenarios*, *Mon. Not. Roy. Astron. Soc.* **382** (Dec., 2007) 1261–1267, [[arXiv:0707.2516](#)].
- [18] M. Grossi, E. Branchini, K. Dolag, S. Matarrese, and L. Moscardini, *The mass density field in simulated non-Gaussian scenarios*, *Mon. Not. Roy. Astron. Soc.* **390** (Oct., 2008) 438–446, [[arXiv:0805.0276](#)].
- [19] A. Pillepich, C. Porciani, and O. Hahn, *Halo mass function and scale-dependent bias from N-body simulations with non-Gaussian initial conditions*, *Mon. Not. Roy. Astron. Soc.* **402** (Feb., 2010) 191–206, [[arXiv:0811.4176](#)].
- [20] R. E. Smith, V. Desjacques, and L. Marian, *Nonlinear clustering in models with primordial non-Gaussianity: the halo model approach*, *ArXiv e-prints* (Sept., 2010) [[arXiv:1009.5085](#)].
- [21] P. Creminelli, L. Senatore, and M. Zaldarriaga, *Estimators for local non-Gaussianities*, *JCAP* **0703** (2007) 019, [[astro-ph/0606001](#)].
- [22] S. Matarrese, F. Lucchin, and S. A. Bonometto, *A path-integral approach to large-scale matter distribution originated by non-Gaussian fluctuations*, *Astrophys. J. Let.* **310** (Nov., 1986) L21–L26.
- [23] D. H. Lyth, C. Ungarelli, and D. Wands, *Primordial density perturbation in the curvaton scenario*, *Phys. Rev.* **67** (Jan., 2003) 023503–+, [[astro-ph/0208055](#)].
- [24] N. Bartolo, S. Matarrese, and A. Riotto, *On non-Gaussianity in the curvaton scenario*, *Phys. Rev.* **D69** (2004) 043503, [[hep-ph/0309033](#)].
- [25] M. Zaldarriaga, *Non-Gaussianities in models with a varying inflaton decay rate*, *Phys. Rev.* **69** (Feb., 2004) 043508–+, [[astro-ph/](#)].
- [26] P. Creminelli and L. Senatore, *A smooth bouncing cosmology with scale invariant spectrum*, *Journal of Cosmology and Astro-Particle Physics* **11** (Nov., 2007) 10–+, [[hep-th/0702165](#)].
- [27] T. Giannantonio and C. Porciani, *Structure formation from non-Gaussian initial conditions: Multivariate biasing, statistics, and comparison with N-body simulations*, *Phys. Rev.* **81** (Mar., 2010) 063530–+, [[arXiv:0911.0017](#)].

- [28] J. Maldacena, *Non-gaussian features of primordial fluctuations in single field inflationary models*, *Journal of High Energy Physics* **5** (May, 2003) 13–+, [[astro-ph/0210603](#)].
- [29] D. Wands, *Local non-Gaussianity from inflation*, *ArXiv e-prints* (Apr., 2010) [[arXiv:1004.0818](#)].
- [30] D. Wands and A. Slosar, *Scale-dependent bias from primordial non-Gaussianity in general relativity*, *Phys. Rev.* **79** (June, 2009) 123507–+, [[arXiv:0902.1084](#)].
- [31] J. Yoo, A. L. Fitzpatrick, and M. Zaldarriaga, *New perspective on galaxy clustering as a cosmological probe: General relativistic effects*, *Phys. Rev.* **80** (Oct., 2009) 083514–+, [[arXiv:0907.0707](#)].
- [32] J. Yoo, *General Relativistic Description of the Observed Galaxy Power Spectrum: Do We Understand What We Measure?*, *ArXiv e-prints* (Sept., 2010) [[arXiv:1009.3021](#)].
- [33] W. H. Press and P. Schechter, *Formation of Galaxies and Clusters of Galaxies by Self-Similar Gravitational Condensation*, *Astrophys. J.* **187** (Feb., 1974) 425–438.
- [34] R. K. Sheth and G. Tormen, *Large-scale bias and the peak background split*, *Mon. Not. Roy. Astron. Soc.* **308** (Sept., 1999) 119–126, [[astro-ph/9901122](#)].
- [35] M. Lo Verde, A. Miller, S. Shandera, and L. Verde, *Effects of scale-dependent non-Gaussianity on cosmological structures*, *Journal of Cosmology and Astro-Particle Physics* **4** (Apr., 2008) 14–+, [[arXiv:0711.4126](#)].
- [36] S. Matarrese, L. Verde, and R. Jimenez, *The Abundance of High-Redshift Objects as a Probe of Non-Gaussian Initial Conditions*, *Astrophys. J.* **541** (Sept., 2000) 10–24, [[astro-ph/0001366](#)].
- [37] M. Maggiore and A. Riotto, *The Halo Mass Function from Excursion Set Theory. III. Non-Gaussian Fluctuations*, *ArXiv e-prints* (Mar., 2009) [[arXiv:0903.1251](#)].
- [38] P. McDonald, *Primordial non-Gaussianity: Large-scale structure signature in the perturbative bias model*, *Phys. Rev.* **78** (Dec., 2008) 123519–+, [[arXiv:0806.1061](#)].
- [39] P. McDonald, *Clustering of dark matter tracers: Renormalizing the bias parameters*, *Phys. Rev.* **D74** (2006), no. 10 103512, [[astro-ph/0609413](#)].
- [40] N. Padmanabhan and M. White, *Calibrating the baryon oscillation ruler for matter and halos*, *Phys. Rev.* **80** (Sept., 2009) 063508–+, [[arXiv:0906.1198](#)].
- [41] M. Manera and E. Gaztanaga, *The local bias model in the large scale halo distribution*, *ArXiv e-prints* (Dec., 2009) [[arXiv:0912.0446](#)].
- [42] H. J. Mo and S. D. M. White, *An analytic model for the spatial clustering of dark matter haloes*, *Mon. Not. Roy. Astron. Soc.* **282** (Sept., 1996) 347–361, [[astro-ph/9512127](#)].
- [43] H. J. Mo, Y. P. Jing, and S. D. M. White, *The correlation function of clusters of galaxies and the amplitude of mass fluctuations in the Universe*, *Mon. Not. Roy. Astron. Soc.* **282** (Oct., 1996) 1096–1104, [[astro-ph/9602052](#)].
- [44] F. Bernardeau, S. Colombi, E. Gaztanaga, and R. Scoccimarro, *Large-scale structure of the Universe and cosmological perturbation theory*, *Phys. Rep.* **367** (Sept., 2002) 1–248, [[astro-ph/0112551](#)].
- [45] P. McDonald, *Clustering of dark matter tracers: renormalizing the bias parameters*, *Phys. Rev.* **D74** (2006) 103512, [[astro-ph/0609413](#)].
- [46] P. McDonald, *Primordial non-Gaussianity: large-scale structure signature in the perturbative bias model*, *Phys. Rev.* **D78** (2008) 123519, [[arXiv:0806.1061](#)].
- [47] D. Jeong and E. Komatsu, *Primordial Non-Gaussianity, Scale-dependent Bias, and the Bispectrum of Galaxies*, *Astrophys. J.* **703** (Oct., 2009) 1230–1248, [[arXiv:0904.0497](#)].
- [48] M. Crocce and R. Scoccimarro, *Renormalized cosmological perturbation theory*, *Phys. Rev.* **73** (Mar., 2006) 063519–+, [[astro-ph/](#)].
- [49] D. Baumann, A. Nicolis, L. Senatore, and M. Zaldarriaga, *Cosmological Non-Linearities as an Effective Fluid*, *ArXiv e-prints* (Apr., 2010) [[arXiv:1004.2488](#)].
- [50] M. H. Goroff, B. Grinstein, S. Rey, and M. B. Wise, *Coupling of modes of cosmological mass density fluctuations*, *Astrophys. J.* **311** (Dec., 1986) 6–14.
- [51] R. Scoccimarro and J. Frieman, *Loop Corrections in Nonlinear Cosmological Perturbation Theory*,

- Astrophys. J. Sup.* **105** (July, 1996) 37–+, [[astro-ph/](#)].
- [52] T. Matsubara, *Resumming cosmological perturbations via the Lagrangian picture: One-loop results in real space and in redshift space*, *Phys. Rev.* **77** (Mar., 2008) 063530–+, [[arXiv:0711.2521](#)].
 - [53] A. Taruya, K. Koyama, and T. Matsubara, *Signature of primordial non-Gaussianity on the matter power spectrum*, *Phys. Rev.* **78** (Dec., 2008) 123534–+, [[arXiv:0808.4085](#)].
 - [54] E. Sefusatti, M. Crocce, and V. Desjacques, *The Matter Bispectrum in N-body Simulations with non-Gaussian Initial Conditions*, *ArXiv e-prints* (Feb., 2010) [[arXiv:1003.0007](#)].
 - [55] E. Sefusatti and E. Komatsu, *Bispectrum of galaxies from high-redshift galaxy surveys: Primordial non-Gaussianity and nonlinear galaxy bias*, *Phys. Rev.* **76** (Oct., 2007) 083004–+, [[arXiv:0705.0343](#)].
 - [56] T. Nishimichi, A. Taruya, K. Koyama, and C. Sabiu, *Scale Dependence of Halo Bispectrum from Non-Gaussian Initial Conditions in Cosmological N-body Simulations*, *ArXiv e-prints* (Nov., 2009) [[arXiv:0911.4768](#)].
 - [57] T. Nishimichi, “private communication.”
 - [58] R. Scoccimarro, E. Sefusatti, and M. Zaldarriaga, *Probing primordial non-Gaussianity with large-scale structure*, *Phys. Rev.* **69** (May, 2004) 103513–+, [[astro-ph/0312286](#)].
 - [59] R. E. Smith, *Covariance of cross-correlations: towards efficient measures for large-scale structure*, *Mon. Not. Roy. Astron. Soc.* **400** (Dec., 2009) 851–865, [[arXiv:0810.1960](#)].
 - [60] D. Schlegel, M. White, and D. Eisenstein, *The Baryon Oscillation Spectroscopic Survey: Precision measurement of the absolute cosmic distance scale*, in *astro2010: The Astronomy and Astrophysics Decadal Survey*, vol. 2010 of *ArXiv Astrophysics e-prints*, pp. 314–+, 2009. [arXiv:0902.4680](#).
 - [61] E. Sefusatti, *1-loop Perturbative Corrections to the Matter and Galaxy Bispectrum with non-Gaussian Initial Conditions*, *ArXiv e-prints* (May, 2009) [[arXiv:0905.0717](#)].
 - [62] R. E. Smith, R. K. Sheth, and R. Scoccimarro, *Analytic model for the bispectrum of galaxies in redshift space*, *Phys. Rev.* **78** (July, 2008) 023523–+, [[arXiv:0712.0017](#)].
 - [63] R. E. Smith, R. Scoccimarro, and R. K. Sheth, *Scale dependence of halo and galaxy bias: Effects in real space*, *Phys. Rev.* **75** (Mar., 2007) 063512–+, [[astro-ph/0609547](#)].

A Standard Perturbation Theory

This appendix reviews the essence of cosmological perturbation theory and serves as a source for the most important equations. For a more detailed treatment we refer the reader to the comprehensive review on the subject by [44]. The evolution equations for the cosmic fluid in an expanding Friedmann-Robertson-Walker Universe can be formulated in terms of the overdensity δ and the velocity divergence $\theta = \nabla \cdot \mathbf{v}$ as

$$\frac{\partial \delta(\mathbf{x}, \tau)}{\partial \tau} + \theta(\mathbf{x}, \tau) = 0 \quad (\text{A.1})$$

$$\frac{\partial \theta(\mathbf{x}, \tau)}{\partial \tau} + \mathcal{H}(\tau)\theta(\mathbf{x}, \tau) + \frac{3}{2}\Omega_m \mathcal{H}^2(\tau)\delta(\mathbf{x}, \tau) = 0. \quad (\text{A.2})$$

A direct solution to this coupled differential equations does not exist. Therefore one has to restrain to a perturbative solution, expanding the density field and velocity divergence in a power series

$$\delta_m(\mathbf{k}) = \sum_{n=1}^{\infty} \delta_{m,p}^{(n)}(\mathbf{k}), \quad \theta(\mathbf{k}) = -\mathcal{H} \sum_{n=1}^{\infty} \theta^{(n)}(\mathbf{k}), \quad (\text{A.3})$$

where $\delta_{m,p}^{(n)}$ and $\theta^{(n)}$ are $\mathcal{O}(\delta_{m,p}^n)$. The solutions for the n -th order contribution to the fields are given by

$$\delta_m^{(n)}(\mathbf{k}) = \int \frac{d^3 q_1}{(2\pi)^3} \cdots \int \frac{d^3 q_n}{(2\pi)^3} \delta_{m,p}(q_1) \cdots \delta_{m,p}(q_n) F_n(q_1, \dots, q_n) \delta^{(D)}(q_1 + \dots + q_n - \mathbf{k}) \quad (\text{A.4})$$

$$\theta^{(n)}(\mathbf{k}) = \int \frac{d^3 q_1}{(2\pi)^3} \cdots \int \frac{d^3 q_n}{(2\pi)^3} \delta_{\mathbf{m},\mathbf{p}}(\mathbf{q}_1) \cdots \delta_{\mathbf{m},\mathbf{p}}(\mathbf{q}_n) G_n(\mathbf{q}_1, \dots, \mathbf{q}_n) \delta^{(\mathbf{D})}(\mathbf{q}_1 + \dots + \mathbf{q}_n - \mathbf{k}), \quad (\text{A.5})$$

where the coupling kernels F_n and G_n can be obtained using recursion relations. For the results presented in this paper we need $F_1 = G_1 = 1$, and

$$F_2(\mathbf{k}_1, \mathbf{k}_2) = \frac{5}{7} + \frac{1}{2} \frac{\mathbf{k}_1 \cdot \mathbf{k}_2}{k_1 k_2} \left(\frac{k_1}{k_2} + \frac{k_2}{k_1} \right) + \frac{2}{7} \left(\frac{\mathbf{k}_1 \cdot \mathbf{k}_2}{k_1 k_2} \right)^2. \quad (\text{A.6})$$

Using the above results, the one-loop corrections to the matter power spectrum read as

$$P_{22} = \int \frac{d^3 q}{(2\pi)^3} P(q) P(|\mathbf{k} - \mathbf{q}|) |F_2(\mathbf{q}, \mathbf{k} - \mathbf{q})|^2, \quad (\text{A.7})$$

and

$$P_{13} = 6P(k) \int \frac{d^3 q}{(2\pi)^3} P(q) F_3(\mathbf{k}, \mathbf{q}, -\mathbf{q}). \quad (\text{A.8})$$